R. & M. No. 3134
(19,900)
A.R.C. Technical Report

MINISTRY OF AVIATION

AERONAUTICAL RESEARCH COUNCIL
REPORTS AND MEMORANDA

Subsonic Wind-Tunnel Tests of Various Forms of Air Intake Installed in a Fighter-Type Aircraft

By

B. J. PRIOR and C. N. HALL

LONDON: HER MAJESTY'S STATIONERY OFFICE
1960
PRICE £1 1*s*. 0*d*. NET

Subsonic Wind-Tunnel Tests of Various Forms of Air Intake Installed in a Fighter-Type Aircraft

By

B. J. PRIOR and C. N. HALL

COMMUNICATED BY THE DIRECTOR-GENERAL OF SCIENTIFIC RESEARCH (AIR), MINISTRY OF SUPPLY

Reports and Memoranda No. 3134*

September, 1957

Summary.—Tests have been made at Mach numbers up to 0·93 in the Royal Aircraft Establishment 10 ft × 7 ft High Speed Wind Tunnel to examine how the longitudinal characteristics of a fighter-type aircraft are affected by the installation of air intakes in the nose, fuselage sides, or wing roots. None of these intakes alters the lift or pitching-moment characteristics significantly, but their effects on external drag vary, and only the nose intake avoids an increase. This superiority derives principally from its low area ratio, the value of which largely determines not only the critical Mach number and hence the behaviour at transonic speeds of the intake fairing but also its sensitivity to spillage and aircraft attitude.

Both forms of divided intake cause an increase in profile drag of roughly 20 per cent; on the side intake this is due to the siting of the boundary-layer by-passes and on the wing-root intake to the increased wing thickness. Their high area ratios make them sensitive to changes in flow direction and lead to high suction levels over the intake fairings which are expected to cause drag increases early in the transonic range. Separation in the canopy-intake junctions of the side intake reduces the drag divergence Mach number to 0·87, compared with 0·89 for the other models.

The shaping of the wing-body junction which was combined with the nose and side intake installations leads to a marked reduction in drag at transonic speed, an advantage not shared by the wing-root lay-out.

1. *Introduction.*—The installation of a turbo-jet engine in an airframe affects the performance of the aircraft in two ways. Internally, the thrust developed by the engine is reduced from the test-bed value by the approach and duct losses; externally, the drag of the aircraft is generally increased by the alteration in shape necessary to house the engine and intake. Any attempt to assess the relative merits of different forms of air intake must therefore take into account both the internal and external losses caused by the installation. Whilst the former have been extensively studied and can now be estimated with fair accuracy at least at subsonic speed[1], relatively little is known concerning the magnitude of the external interference set up by the different classes of intake.

The present tests were undertaken in 1952 to make good this deficiency by comparing the aerodynamic characteristics of four models of the same basic aircraft, each model differing from the others only in the type of air intake installed. The first model did not have an intake represented and was tested to provide a standard with which the results obtained on the ducted models could be compared. On the other models, the intake was housed in the nose, fuselage side, and wing root respectively, the internal ducting behind the entries being idealised in each case.

* R.A.E. Report Aero. 2576, received 6th March, 1958.

A general view of each design is given in Figs. 1a to 1d. The proportions of the basic aircraft conform closely with the values typical of current practice on single-jet fighters. This choice was made because the high thrust/weight ratio and the limited space available makes the design of an efficient air-intake system for this class of aircraft most difficult.

The changes in external shape of the body or wing required to house the ducts gave scope for further modifications designed to raise the critical Mach number of the aircraft and to reduce the transonic drag. Thus with the nose and side intake models, the increased width of body made possible the adoption of the waisted wing-body junction shape, known to be beneficial at transonic speeds[2]; on the wing-root intake model, the sweepback of the maximum-thickness line was considerably increased over the centre-section of the wing in an attempt to compensate for the greater wing thickness needed for the ducts. Where appropriate, a by-pass was provided on the models to divert the fuselage boundary layer from the air intakes. This was done not so much to reduce the losses inside the model ducts, but rather to obtain a realistic value of external drag, to which the by-pass may contribute appreciably[3]. In order to estimate the internal losses, pitot and static pressures were measured in the jet exit plane.

Each intake model was tested over the same ranges of incidence, Mach number and mass flow. Apart from the overall forces, detailed pressure distributions over the intake lip fairings were obtained to help in interpreting the force measurements.

2. *Design of Models.*—2.1. *General Considerations.*—The basic wing-fuselage configuration was chosen to be representative of a fighter aircraft (at 1/12 scale) with a critical Mach number of about 0·9, *i.e.*, within the test range of Mach number of the High Speed Tunnel. The wing section used was a Thwaites 9 per cent (Table 6), with 38·6 deg of sweepback on the quarter-chord line, and the aspect ratio was 3·15; the leading dimensions of each model are listed in Table 5. The tail unit was omitted from the design, but a cockpit canopy was included since this was expected to create interference effects, particularly in the side-intake configuration.

The air intake and fuselage proportions are those suitable for a single axial turbo-jet engine of the R.A.14 type: the minimum fuselage diameter is 4·38 ft full scale, and the intake throat area (3·784 sq ft full scale) was chosen so that the entry Mach number would not be greater than $M = 0{\cdot}55$ with this engine running at cruising r.p.m. The ducting begins with a representative rate of expansion from the throat ($2\frac{1}{2}$ per cent per foot full scale, equivalent cone angle $1\frac{1}{2}$ deg), but reaches a maximum area of only 1·1 × throat area, subsequently reducing smoothly to the required exit nozzle area. Three exit nozzles were designed, providing values of intake velocity ratio (V_i/V_0 = inlet velocity ÷ free stream velocity) appropriate to high-speed flight, *viz.*, 0·5, 0·65 and 0·8; a fourth, to give zero flow, closed the exit nozzle with a conical fairing.

2.2. *Design of Intake Lip Fairings.*—Before attempting to design the three different intake configurations of this test, a study was made of the design methods of Küchemann and Weber for circular intakes in ' Aerodynamics of Propulsion '[4], and of the National Advisory Committee for Aeronautics (U.S.A.) in ' The Development and Application of High-critical-speed Nose Inlets '[5]. In both of these it is evident that the most important parameter in any design is the ' area ratio ' of the intake (*i.e.*, throat area ÷ maximum external cross-sectional area), since this determines the frontal area that is available to carry the thrust force on the intake fairing. For lower area ratios this frontal area is greater, and it is possible to maintain lower levels of suction coefficient over lip fairings of good shape and thus raise the critical Mach number of the intake. Other design factors of importance are the length or fineness ratio of the lip fairing, and the sharpness of the lip shape, both of which effect the distribution of velocity over the intake and also determine its sensitivity to off-design conditions (high incidence, large spillage, and the static condition).

In Ref. 4 Küchemann and Weber have formulated a series of related lip fairings for circular intakes, Classes A, B and C*, whose inner and outer surfaces are formed from two elliptic quadrants meeting on the ' capture line '; the variation of their properties with area ratio is shown

* The Küchemann lip fairings are defined by their Class and their area ratio in per cent, *e.g.*, A-18.

in Fig. 5. The three classes provide a choice of lip shape, and their lengths have been designed to be close to those of the optimum contours which produce a uniform velocity over the whole outer surface; the Class A is the bluffest fairing of the series for a given area ratio, and is therefore the least sensitive to variations in the position of the stagnation point but has the lowest critical Mach number; the Class C is the sharpest fairing, and thus achieves the highest critical Mach number for a given area ratio, under optimum conditions. The theoretical critical Mach numbers of Fig. 5 tend to be conservative for Classes A and B, and may be exceeded before there is any marked rise in drag.

In Ref. 5 the N.A.C.A. 1-series* of lip fairings for circular intakes was developed. In this series there is only one fairing shape: the outer surface is rather flatter than a quarter-ellipse, and the inner lip is formed from a circular quadrant whose radius is kept small for all area ratios (*see* Fig. 5). The length of the fairing is obtained from a selection chart for the combination of area ratio and minimum velocity ratio of the particular intake specification.

In the design of the individual intake configurations for these tests, the need to obtain a good off-design performance as well as a good high-speed performance was continually kept in mind. To obtain a high critical Mach number a relatively sharp fairing shape with a high fineness ratio is desirable (Fig. 5), but a bluff fairing is much less sensitive to changes in flow conditions, as is clear in the Table below which gives static inflow losses measured on pitot intakes using these fairings. The measurements[4, 6] were made over a range of intake flows, the inlet being unchoked:

TABLE 1

Static Inflow Losses

	Area ratio (per cent)	Inner lip thickness ÷ throat radius	Static inflow loss $\Delta H/\frac{1}{2}\rho V_i^2$ (per cent)
Class A	25 to 50	0·15	2 to 4
Class B	25 to 50	0·10	10 to 20
Class C	25 to 50	0·03	20 to 40
N.A.C.A. 1–70–200 ..	49	0·01	50 to 60

These conflicting requirements are more easily satisfied in the case of intakes having a low area ratio, when a good compromise is possible.

2.3. *Datum Model.*—This model has a simple streamline cylindrical body with no intake (Fig. 2a) and was included in the tests to provide a standard of comparison against which the effects of the installation of the air intakes and consequent deformation of the basic fuselage or wing shape of the other models could be measured. For simplicity the jet exit nozzle was faired over, in preference to having a nozzle with a bluff end and then attempting to correct for differences in base pressure and afterbody drag.

Full-chord pressure measurements were made at the wing root ($\eta = 0{\cdot}13$) and at $\eta = 0{\cdot}61$ (away from centre and tip effects) to establish the critical Mach number of the wing and for subsequent comparison with the pressure distribution over the fairing of the wing-root intake.

2.4. *Nose-intake Model.*—The ' waisted ' wing-fuselage intersection incorporated in this model (Table 9, Fig. 2b) was calculated by Küchemann's vortex-ring method[7] for a Mach number of 0·94. It was designed to maintain the sweepback of the wing isobars right up to the fuselage side, at zero lift.

* Circular intakes of the N.A.C.A. 1-series are described in terms of their proportions. Thus the N.A.C.A. 1–50–200 has a ratio of intake diameter to external diameter of 50 per cent (therefore area ratio = 25 per cent), and a ratio of total fairing length to external diameter of 200 per cent.

The elliptic fuselage cross-sections resulting from the fuselage waisting led to an elliptic intake for this model, and the intake plane was staggered at 15 deg from the vertical in order to equalise the suction levels above and below the intake at a positive angle of incidence (Fig. 2b). The overall area ratio of the intake is 18 per cent, which results in a high critical Mach number for any of the lip fairings:

TABLE 2

Critical Mach Numbers for Fairings of Area Ratio 18 *per cent*

	Critical Mach number for V_d/V_0 = 0·5	0·8	L/T
Class A–18, B–18 ..	0·82 to 0·83	0·83	6·35
Class C–18	0·86	0·86	7·12
N.A.C.A. 1–42–210 ..	0·88	0·88	7·30

As a result it is possible to use the Class A and B sections, with their desirable off-design characteristics, and suffer only a small reduction in the critical Mach number of the intake. The fairing at the horizontal section (DD) is a B-18 fairing with its fineness ratio increased (L/T = 7·23) to raise its critical Mach number to the level of the Class C and N.A.C.A. fairings. The lower lip is closely similar to this (*see* Fig. 4a), but on the upper lip (section CC) the effects of incidence were further reduced by providing greater thickness, and the ratio of inner to outer lip thickness is that for an A-18 fairing (Fig. 5). All the outer surface fairings end at the same station on the fuselage.

The internal ducting divides at about one mean entry diameter behind the intake to pass on either side of the balance compartment (Fig. 2b). Pressure measurements were made along all three sections CC, DD and EE, although on section CC the cockpit canopy limited these to the first 40 per cent of the fairing length.

2.5. *Side-intake Model.*—The side intake was combined with a waisted body shape which was identical with that of the nose intake design. The intake position, the fuselage width between the intakes, and the height of each intake were made representative of current practice (Fig. 2c): the position ratio of the intake (*i.e.*, approach surface area ÷ intake area) is $8\frac{1}{2}$, and the area ratio (based on the equivalent circular intake) is 55 per cent. This high area ratio follows immediately from the large amount of frontal area taken up by the cockpit, and it could only be lowered by reducing the cockpit width or having an excessive increase in the maximum fuselage cross-sectional area. Because of the high area ratio, the critical Mach numbers for the different types of lip fairing are low (even for the N.A.C.A. fairing the critical Mach number is well below that of the wing), and the well-rounded fairings are severely penalised :

TABLE 3

Critical Mach Numbers for Fairings of Area Ratio 55 *per cent*

	Critical Mach number for V_d/V_0 = 0·5	0·8	L/T
Class B–55	0·62	0·64	1·70
Class C–55	0·71	0·73	2·66
N.A.C.A. 1–74–60 ..	0·76	0·76	4·61

Thus only a poor compromise between the conflicting design requirements is possible.

The thickening of the intake lip at section FF due to the geometry of the lay-out (Fig. 4b) is helpful in that it tends to lower suction levels above the intake at positive incidence, and it was decided to use a C-55 fairing here. By keeping a constant fairing length round the intake, the fineness ratio of the fairing at section GG was raised to $L/T = 3{\cdot}79$, in an attempt to increase its critical Mach number. The inner lip thickness is $0{\cdot}03$ of the throat radius, as for any Class C fairing on a circular intake.

The boundary-layer by-pass was designed to take the full boundary layer at the appropriate local Reynolds number of the test, and the by-pass area is nearly a sixth of the intake area (slightly large compared with the needs at full-scale Reynolds numbers). A flat on the fuselage side led into the by-pass duct itself, which divided into two to discharge this ' dead ' air both above and below the intake (Figs. 2c and 18a). Pressure measurements were made over the intake lips at the two sections FF and GG, and extended two fairing lengths at each of these sections.

2.6. *Wing-root Intake Model.*—The design of this model aimed to improve the critical Mach number of the basic wing, and to offset the root thickening necessary to house the intake, by increasing the sweepback of the maximum-thickness line of the wing over the modified inboard sections (Fig. 2d). Windwise sections across this region are all smooth aerofoil shapes. Thus this design differs from the Hawker *Hunter* intake lay-out, in which the wing modification is kept to the minimum necessary to house the intake and duct with the result that the line of maximum thickness across the intake fairing is unswept and windwise sections there contain a discontinuity. Tests have shown that this type of lay-out can lead to flow separations, giving an unnecessarily large increase of drag due to the installation.

It was considered that the thickness/chord ratio of the wing at the fuselage side should not exceed 16 per cent, which is the maximum on the *Hunter* wing-root. This led to two-dimensional area ratios across the intake (local intake depth ÷ local wing maximum thickness) of the order of 50 per cent and thus, almost inevitably, to relatively low critical Mach numbers and therefore to the choice of the Class C fairing. However, in this design the sweepback across the wing-root should raise the critical Mach numbers by about $0{\cdot}05$ above the values indicated in Fig. 5.

The wing sections across the modified wing-root were formed from front and rear fairings meeting at the position of maximum thickness (Table 8). The rear fairing was designed to give an increased wing thickness while keeping to the same trailing-edge angle as the basic wing section, and was evolved through a series of calculations of its pressure distribution when combined with an elliptic nose, the main aim being to prevent the occurrence of a secondary suction peak towards the rear of the section. The forward fairing was a quarter-ellipse, and formed the intake lip; by careful choice of the proportions of the intake and the sweepback of the line of maximum thickness, the length of this fairing at any section was made to approximate to the length (as given by Fig. 5) of the Class C fairing appropriate to the local (two-dimensional) area ratio of that section (Fig. 4b). Fig. 5 is based upon the properties of circular intakes, and so the choice of lip length is a compromise between a two-dimensional design, which produces too bluff a fairing, and a three-dimensional approach which the intake geometry does not appear to justify. The compromise resulted in a sweepback of 58 deg for the line of maximum thickness across the wing-root (*cf.* 36 deg on datum wing), and local area ratios from 60 per cent (at the fuselage side) to 25 per cent. It was expected that the suction peak caused by the poor area ratio at the fuselage side would be alleviated by the ' centre effect '.

The intake was formed by cutting back the basic leading edge, thus lowering its sweepback from over 43 deg to 17 deg and giving a position ratio of $8\frac{1}{2}$; the lips were staggered at 15 deg to offset the effects of wing circulation under lift and reduce the upper-surface velocities. The inner lip radius was kept constant across the intake at the value given for a Class C fairing by Fig. 5 for the local area ratio of section HH, *i.e.*, it is generous for sections further outboard; it is greatly increased at the outer corner of the intake, which was kept well rounded (Fig. 4b) to avoid large static losses[8].

As in the side-intake design, a boundary-layer by-pass was included, but in this case, for constructional reasons, it could not be divided between upper and lower surfaces, and it was vented entirely on the upper surface. This proved to be an undesirable feature, and is discussed in Section 5.2.

As a matter of interest, the axial distribution of cross-sectional area of the four models is compared in Fig. 3, although the transonic area rule was not used in the design of these models. The smoothest area distribution results from the use of the waisted wing-body junction in combination with the nose intake; in the wing-root intake model, of course, the design attempted to improve the wing-body junction entirely by wing-section modifications, and the rates of change of area in this model are much more abrupt.

3. *Experimental Details.*—3.1. *Model Support.*—The major difficulty involved in the testing of ducted models at high subsonic speeds is that of supporting the model without undue interference with either external or internal airflows. In these tests fairly precise values of inlet velocity ratio had to be obtained without too high a value of internal drag ; it was therefore considered better to leave the ducts unobstructed. This was achieved by housing the drag balance, to which the model was attached, in the cockpit space between the two branches of the duct; the balance was mounted in a socket in the front end of the sting, which was then brought out through the underside of the body and carried aft beneath the rear fuselage (Fig. 6a). The objection to this arrangement lies in the interference set up beneath the model. This was not thought to be critical in the present tests, where the emphasis was placed more on comparative than absolute results.

3.2. *Model Construction.* The datum model had no internal duct system and was therefore the most straightforward to build. The wings were made separately of Hydulignum, as this simplified the insertion of the pressure-plotting lines. The body was made of laminated teak in two portions, which fitted together round the roots of the wings after these had been assembled onto the drag balance.

The three ducted models were all similar in construction, so that only one, the side intake, is described in detail (Fig. 6a). Each wing and half-body was formed integrally from light alloy, the external surfaces of the wing and inner surface of the duct being shaped on a profile milling machine. After machining, the duct sections were closed by thin cover plates which formed the inner walls of the ducts. To each half of the model was added the appropriate nose portion made of laminated teak (Fig. 18a); this simplified the shaping of the by-pass passages, which were hollowed out of its sides. Each sub-assembly then fitted onto the drag balance, and the model was completed by adding the wooden afterbody with the appropriate exit nozzle.

The measurement of surface pressures at close intervals round the thin intake lip fairings required a special method for inserting the pipelines. These were embedded in a transparent matrix of Araldite, and the hole was obtained by drilling into the tube after the resin had hardened. Near the lips of the fairings 1-mm-diameter tubing had to be used, and with these the mouth of each tube was plugged with a close-fitting nylon thread while the Araldite was applied, and the thread was extracted after this had set. The pipelines passed through a slot in the body into the balance compartment, where they were arranged round the sting before being led out through the under-surface of the body.

3.3. *Drag Balance.*—The drag or, more exactly, the axial force, was measured by the strain-gauge balance illustrated in Fig. 6b. The balance consists of an upper beam to which the model is bolted, and a lower beam attached to the sting; three flexible uprights transmit normal forces from the model to the sting, while the axial forces are carried by the two horizontal strips, on which the strain-gauges are mounted (Fig. 6b). The strain in these strips is $2{\cdot}3 \times 10^{-6}$ per lb, which with the electronic equipment at present in use enables 0·05 lb to be detected. Calibration showed that interference from normal force was not significant, at least over the range of travel of the centre of pressure encountered during the tests. Considerable difficulty was, however,

experienced with temperature drift, and this limited the experimental accuracy especially at low speed. An investigation into the cause of this drift established that its magnitude and even its sense were determined by the properties of the individual gauges rather than by the design of the balance.

3.4. *Range of Tests.*—The four models were tested in the 10 ft × 7 ft High Speed Wind Tunnel at intervals between November, 1953, and August, 1954. The tests were made at a series of Mach numbers ranging from 0·40 to 0·93, at a constant Reynolds number of 1·1 million (based on the standard mean chord). Only a moderate range of lift coefficient was covered, since any attempt to determine the effect of intake performance on stalling behaviour would have seriously aggravated the problems associated with model construction. The ducted models were tested at velocity ratios of 0*, 0·50, 0·65, 0·80 and in addition the tests on the side-intake and wing-root intake models at $V_i/V_0 = 0{\cdot}65$ were repeated with the boundary-layer by-passes faired over.

Each model had to be tested twice; once to measure the pressures round the intake lip fairings and at the duct exit, and again to measure the forces after the pressure connections had been removed. Normal force and pitching moment were measured by means of strain-gauges mounted at two positions on the sting, while the axial force was obtained from the balance described in Section 3.3.

TABLE 4

Range of Tests ($R = 1{\cdot}1 \times 10^6$)

Model	By-pass condition	Velocity ratio				Range of Mach number	Range of incidence (deg)
Datum	—	—				0·40 to 0·93	−2 to +9
Nose intake ..	—	0	0·50	0·65	0·80	0·40 to 0·93	−2 to +9
Side intake ..	Open	0	0·50	0·65	0·80	0·40 to 0·93	−2 to +9
	Sealed	—	—	0·65	—	0·40 to 0·93	−2 to +9
Wing-root intake	Open	—	0·50	0·65	0·80	0·40 to 0·93	−2 to +9
	Sealed	—	—	0·65	—	0·40 to 0·93	−2 to +9

4. *Corrections and Presentation of Results.*—4.1. *Corrections to Results and Experimental Accuracy.*—The change in free-stream direction caused by the constraint of the tunnel walls was estimated assuming elliptic loading across the span and values of model incidence were then corrected according to the equation

$$\Delta\alpha^\circ = 0{\cdot}27C_L .$$

A further correction was made to incidence to allow for the deflection of the sting under load; this was measured, and the following relationship derived:

$$\Delta\alpha^\circ = 0{\cdot}001N + 0{\cdot}0026M ,$$

where N is the force acting normal to the sting (lb) and M is the pitching moment about an axis at $0{\cdot}295\bar{c}$ (lb ft).

* Except on the wing-root intake owing to shortage of time.

The total correction to incidence did not exceed 0·5 deg for these tests and values of incidence are considered accurate to $\pm$ 0·05 deg.

The increase in free-stream velocity at the model position due to its blockage was estimated by the method developed by Evans[9] and appropriate corrections were then applied to the observed values of Mach number, dynamic and static pressures. The highest correction to Mach number was 0·025 and the values quoted should be accurate to $\pm$ 0·003.

The main source of error in the strain-gauge readings was the zero drift caused by the rise in tunnel temperature. This changes most rapidly when the tunnel is cold, and an effort was made to reduce the drift by raising the air temperature in the tunnel before taking readings. As a further precaution two thermo-couples were installed, one on the drag balance and the other on the sting. These enabled the variation of zero readings with local gauge temperatures to be determined, and the necessary correction to be applied. All force coefficients should therefore be correct within $\pm$ 0·001, although the results at high speeds are likely to be better owing to the greater magnitude of the quantities measured. The pressure measurements were taken on a multi-tube manometer filled with alcohol reading to $\pm$ 0·05 in.; this is equivalent to roughly $\pm$ 0·001 in C_p over the upper half of the speed range.

4.2. *Support Interference.*—The presence of the supporting sting underneath the fuselages of the models interferes with the flow in that vicinity. Some idea as to the extent of this interference at low Mach number is given by Figs. 31a and 31b, where the pressure distributions calculated by Küchemann's method[10, 11] for the wing-root section (AA) and the mid-semi-span section (BB) at incidences of 0 deg and 2 deg and neglecting the effects of compressibility, are compared with the results obtained on the datum model at $M = 0{\cdot}4$. The interference is greatest on the lower surface of section AA, where the inclined portion of the sting increases the pressures over the front part of the section and causes an expansion to occur locally near $x/c = 0{\cdot}6$. On the upper surface the pressure distribution is more regular although the local pressures near the leading edge are less than those on the lower surface, suggesting that the sting distorts the flow direction here to an extent equivalent to roughly 1 deg in incidence.

The good agreement obtained between the calculated and measured values for section BB confirms that the interference is confined to a region at the wing root. The distributions measured over section AA at Mach numbers above 0·4 show similar effects (Figs. 21a and 12b) although the magnitude of the interference is clearly greater.

The effect of the interference is noticeable on both the pitching moment and the drag curves. Thus a positive value of C_{m_0} is obtained on all the models, the value varying from 0·01 at $M = 0{\cdot}40$ to 0·03 at $M = 0{\cdot}91$ (Fig. 8), and although this is partly accounted for by the pressure field round the cabin, sting interference must also be partly the cause (Fig. 12). Again, the drag curves given in Fig. 9a show that minimum drag occurs at a positive value of C_L, which increases with Mach number. This asymmetry arises through the variation with incidence in the interference drag. The latter is greatest at negative incidence owing to the higher velocity round the inclined portion of the sting beneath the fuselage, and then falls progressively as the incidence increases (positively). The presence of the sting therefore reduces the drag divergence Mach numbers of all the models by an amount which lessens as the incidence is raised. The magnitude of the interference, though appreciable at supercritical Mach numbers, does not appear to mask the differences between the drag characteristics of the various models, and the results should therefore provide a fair basis of comparison.

4.3. *Presentation of Results.*—The results are discussed in three main Sections. The first (Section 5.1, Figs. 7 to 17), compares the characteristics of the models at a velocity ratio of 0·65 over the range of Mach number covered by the tests, using the available pressure distributions to explain the differences brought about by the three types of intake layout. The second (Section 5.2, Figs. 18 to 22), deals with the effect of the boundary-layer by-passes on the side and wing-root intakes, while the last describes how the different forms of intake are affected by spillage, incidence, and lip stagger (Section 5.3, Figs. 23 to 30).

5. *Discussion of Results.*—5.1. *Relative Performance of the Different Intake Models.*—The force comparisons between the four models made below are all for a velocity ratio of 0·65, with the by-passes of the side and wing-root intakes operating. However, the pressure distributions used to illustrate the changes caused by the installation of the wing-root intake (Figs. 11a and 16) refer to conditions with the by-passes sealed. This is because the efflux from the by-passes in this particular design cause local perturbations to the pressure distributions (Fig. 22), which tend to mask the effects of the wing-root modifications.

5.1.1. *Force measurements.*—The lift and pitching-moment characteristics of the models are shown in Figs. 7 and 8. Installation of the intakes has raised the lift divergence Mach number from 0·89 to between 0·9 and 0·91, a result which suggests that the changes incorporated in the wing-body junctions are beneficial at small lift coefficients, even though they were designed for zero lift; it also causes a slightly greater variation of C_{m_0} with Mach number, though this asymmetry is mainly caused by the canopy and the sting support (Section 4.3), and at high Mach number it reduces the severity of the small 'pitch-up' which is evident on the datum model. In general, however, variation of intake position on this aircraft has little effect upon its lift and pitching-moment characteristics.

The variation of gross drag (*i.e.*, the sum of external and internal drag) with Mach number for the four models is shown in Figs. 9a and 9b. The use of gross drag, rather than external drag, is justified by Figs. 10a and 10b which show the values of internal drag (based on wing area and calculated by the method of Appendix I) at low and high Mach number for all flow conditions. The cleanness achieved in the internal ducting has resulted in very small internal losses, so that differences in internal drag between the models are insignificant in the comparisons of gross drag of Fig. 9.

The drag divergence Mach number ($\Delta C_D = 0{\cdot}005$) of the datum model is 0·89 at $C_L = 0$ and the values for the nose and wing-root intake models are closely similar, but for the side-intake model it is lowered by 0·02 due to an additional drag rise commencing at $M = 0{\cdot}77$. For $M < 0{\cdot}89$ the side and wing-root intakes are alike in causing a considerable increase in profile drag over the datum model (about 20 per cent at low lift), but the nose intake has in fact achieved a slight reduction of drag in spite of the increase in frontal area. For $M > 0{\cdot}89$ the grouping is changed, and the side and nose-intake designs show a marked reduction in the rate of increase of drag, with the promise of substantially less transonic drag, when compared with the datum and wing-root intake models, owing to the fuselage waisting incorporated in these designs.

Thus the nose-intake design is distinctly the most successful over the full Mach-number range, the inclusion of the intake having been achieved without detriment to the design, and in fact the combination of this intake lay-out with the fuselage waisting has produced a model with markedly less drag at speeds in the transonic range. The higher drag of the side-intake model throughout the test range is almost entirely due to the boundary-layer by-pass (Fig. 19), which, of course, is an essential feature of the lay-out, although at full scale and with careful design (*see* end of Section 5.2), it should be possible to reduce this penalty considerably. At moderate Mach numbers (less than 0·8) in the absence of the by-pass, the side intake would be almost as good as the nose intake as regards its external drag, and for $M > 0{\cdot}92$ the benefits conferred by the waisted fuselage are sufficient to show an improvement in drag over the datum model even with this by-pass in operation. The aerofoil modification of the wing-root intake model has been successful in maintaining a drag divergence Mach number almost as high as the datum model, but it has not prevented a considerable increase in profile drag due to the installation of the intake (which is only partly accounted for by the by-pass (*see* Fig. 21b)) and it does not reduce transonic drag in the same way as the waisted wing-body junction.

5.1.2. *Measurements of pressure distribution.*—Understanding of the drag characteristics of the different intake designs is greatly aided by the pressure distributions measured during the tests. Some of these are presented in Figs. 11 to 17.

Pressure distributions measured on the datum model wing are shown for incidences of 0 deg and 4 deg in Fig. 12. The pressure distribution over section BB ($\eta = 0{\cdot}61$, Figs. 12c and 12d) show that the flow over the wing is first affected by a shock wave at about $M = 0{\cdot}88$ at $\alpha = 0$ deg; this is confirmed by the sudden decrease of the trailing-edge pressure at this Mach number (Fig. 13)*. The asymmetry evident at zero incidence on section AA ($\eta = 0{\cdot}13$, Fig. 12a) is a measure of the strut interference present on all these models (Section 4.3).

The variation of pressure distribution with increasing Mach number over the nose, side and wing-root intakes at the two incidences of 0 deg and 4 deg are shown in Figs. 14, 15 and 16 respectively.

Over the whole of the nose intake there is a nearly uniform velocity distribution, which is disturbed only by the canopy and wing, and by the stagger of the intake which is effective in offsetting the increased suctions on the upper lip at incidence. The intake is therefore, as a result of its low area ratio, very close to the optimum design condition of uniform velocity distribution (which would give the highest possible critical Mach number), in spite of the well-rounded nose shapes used in this design. A supersonic region is first formed on the lower lip at $M = 0{\cdot}84$ ($\alpha = 0$ deg.), but this does not spread round the whole circumference of the intake until $M = 0{\cdot}90$, and even then there are no severe shock waves present. Thus the installation of this intake does not lower the critical Mach number of the aircraft at all. The relatively bluff lip sections used avoid high peak suctions due to changes of incidence, and the lowest critical Mach number falls only to $M = 0{\cdot}81$ when $\alpha = 4$ deg ($C_L = 0{\cdot}26$).

It is of interest to note the small region of supersonic flow that develops towards the rear of section DD (Fig. 14); longitudinally this coincides with the maximum bulk of the canopy, suggesting that the pressure field round the canopy is affecting the pressure distribution here at high Mach number (the critical Mach number of the canopy is estimated to be 0·8 from the low-speed pressure measurements of Ref. 13).

The velocities over the side intake (Fig. 15) are very much higher than those on the nose intake (*see* comparison of Fig. 11b), as a result of the high area ratio of this design. Sonic speed is reached over the full circumference of each intake at $M = 0{\cdot}70$; at higher speeds the supersonic region extends rearwards and a clearly defined shock wave is present at $M = 0{\cdot}8$ to the rear of the intake fairing, producing the additional drag rise noted in Fig. 9b. Near the top of the intake the region of high velocities is more extensive than on the horizontal section at $\alpha = 0$ deg (Fig. 15a), particularly at the higher Mach numbers; the difference in velocity level is no doubt in part due to the increased bluffness of this section, but it seems that interference from the canopy is also partly responsible, and that the less clearly defined shock wave and poor pressure recovery on section FF for $M = 0{\cdot}85$ is caused by a separation in the canopy-intake junction due to the shock wave from the canopy. The lip fairings used on this intake are much more sensitive to incidence than are those of the nose intake, and at $\alpha = 4$ deg the critical Mach number of section FF falls to $M = 0{\cdot}6$ (Fig. 15b).

The installation of the wing-root intake has considerably affected the pressure distribution in its vicinity (Fig. 11a), and even at $\alpha = 0$ deg a suction peak is formed on the intake lip. The intake is highly sensitive to the local flow direction, so that even at zero incidence there are high velocities over the intake lip as a result of pre-entry retardation and interference from the sting support (*see* Section 4.2). The suction peak is highest at the inboard end of the intake (*see* Fig. 16a, which shows the upper surface pressures, by-pass duct sealed), where the area ratio is also highest, and it is apparent that the design expectation that the centre effect would counterbalance the increased area ratio here has not been realised. A study of the local isobar pattern shows that there is an effective sweepback of 35 deg over the intake lip, and sonic velocity is reached locally at $M = 0{\cdot}76$ close to the fuselage, the supersonic region spreading outwards to cover the whole intake when $M = 0{\cdot}85$; the comparatively sharp lips used in an attempt to compensate for the

* Pearcey has shown in Ref. 12 that this 'divergence' of the trailing-edge pressure indicates when the effects of shock-induced separation become important, the separation having caused the pressure rise through the shock wave to be so reduced that the velocity immediately behind the shock wave is just sonic.

low critical Mach number due to the poor area ratio of this intake, combined with the effects of the wing circulation, make the intake even more sensitive to incidence than the side intake, and at $\alpha = 4$ deg the critical Mach number falls to about $M = 0{\cdot}6$ over the whole intake. However, this local shock wave on the intake lip does not appear to cause any noticeable increase in the total drag of the aircraft, and examination of the trailing-edge pressures on section II at $\alpha = 4$ deg (Fig. 16b) suggests there is no flow separation behind the intake until $M > 0{\cdot}88$.

5.1.3. *Intake critical Mach numbers.*—The variation with Mach number of the maximum suction values occurring on the ten sections on which pressure distributions have been measured are shown in Fig. 17, thus enabling the range of critical Mach numbers on each intake to be determined. The low levels of suction maintained on the nose intake, and the benefits of sweepback to the wing-root intake are at once apparent. The critical Mach numbers indicated on this Figure are in good agreement with the estimates shown in Tables 2 and 3.

It should be borne in mind that, although increase of Mach number above the critical does imply the development of local supersonic velocities, as long as the shock waves remain well forward and do not provoke separated flow there need be no noticeable drag increase. In the case of the side-intake model, where separation occurs between the canopy and the intakes, a small drag increase was in fact noted (Section 5.1.2) at supercritical Mach numbers.

The high suctions observed over the side and wing-root intakes, which result from their high area ratio, have had no seriously adverse effects under the conditions reviewed so far in this section. However, at moderate supersonic speeds the thrust realised on the intake surfaces becomes an important part of the total thrust produced by the engine (40 per cent at $M = 1{\cdot}2$ (*see* Ref. 4, para. 8.5)), and for any particular velocity ratio at such speeds the thrust available from the intakes of these two designs may fall off at a lower Mach number than in the case of the nose intake, where the surface velocities are much lower.

5.2. *Effects of the Boundary-layer By-passes on the Side and Wing-root Intakes.*—The value of a boundary-layer by-pass cannot be assessed purely on the basis of these model tests. For although the changes in internal and external drag due to sealing the by-passes can be measured, the idealised internal ducting used for these models makes it impossible to determine the loss in engine thrust which would result on a full scale installation, where there is a much greater rise in pressure between the intake and the compressor face, with the attendant risk of separation. The changes in internal drag actually measured are very slight (Fig. 10), and the following discussion is concerned with the effect of by-pass operation on the gross drag of the models.

5.2.1. *Side intake.*—A detailed view of the side-intake model showing the position of the boundary-layer by-pass is given in Fig. 18a; the close proximity of the upper by-pass exit to the cockpit canopy should be noted. On this model no change in either the lift or pitching-moment characteristics was detected when the by-passes were faired over. Curves of drag coefficient against Mach number, however, show an increase in drag coefficient due to by-pass operation of about $0{\cdot}0035$ at $M = 0{\cdot}60$ and $0{\cdot}001$ at $M = 0{\cdot}93$ (Fig. 19).

By-pass drag can be divided into two parts: internal and external. Internally, drag is caused by turning the by-pass flow through 90 deg; externally, some further drag may result from the interference with the airflow near the exits*. For the model the magnitude of the first term can be roughly estimated by assuming that the velocity at entry into the by-passes is the same as that into the intakes; neglecting compressibility, this gives $\Delta C_D = 0{\cdot}0015$ for a velocity ratio of $0{\cdot}65$.

The difference between this term and the measured increase in drag coefficient of $0{\cdot}0035$ at $M = 0{\cdot}60$ is therefore caused by the efflux; this term evidently falls with increase in Mach number. A comparison of the pressure distributions measured at section FF on the shoulder of the intake

* On an aircraft this is usually reduced by fitting exit louvres, so that the flow emerges more nearly in a streamwise direction.

fairing with the by-passes open and sealed (Fig. 20) gives an indication of the form of the external interference set up by the efflux, even though the section is too local to provide a complete picture. At low Mach numbers, operation of the by-passes worsens the pressure recovery over the rear part of the fairings, but improves it at higher Mach numbers. The apparent fall in by-pass drag above $M = 0{\cdot}85$ is thus seen to be due to the fact that separation in the canopy-intake junction occurs at high Mach number even when the by-pass is sealed, whilst at lower Mach numbers, separation occurs only when the by-pass is operative.

5.2.2. *Wing-root intake.*—Unlike the side-intake design, the by-pass ducts on the wing-root intake were not divided into upper and lower sections, and the whole of the by-passed flow was discharged through exits lying flush with the upper surface of the wings (Fig. 18b). Minor changes were found in the lift and pitching-moment characteristics due to by-pass operation but no significant increase in drag (Fig. 21). The by-passes cause a loss in lift which is very slight at $M = 0{\cdot}40$ but becomes more noticeable at higher speeds particularly at values of $C_L > 0{\cdot}45$; at $M = 0{\cdot}91$ the loss in lift has a destabilising influence on the pitching-moment curve which implies that it is centred over the rear part of the wing. In contrast with the side-intake results, the rise in drag coefficient due to by-pass operation is scarcely perceptible over the lower part of the speed range and amounts to about $0{\cdot}001$ at low lift for Mach numbers above $0{\cdot}85$. Evaluating the internal drag of the by-passes as before gives a value of ΔC_D of $0{\cdot}0010$, so that the external or interference drag is negligible in this case. The pressure measurements made over the intake lip fairings are well sited to detect any disturbance set up by the efflux, and all three sections (HH, II, JJ in Fig. 22) show that it raises the pressures towards the leading edge of the wing and lowers them for a short distance aft of the by-pass exit. The perturbations are greatest close to the by-pass exit (section HH) and increase with Mach number, but even at $M = 0{\cdot}91$ the distribution over section II is affected only up to $x/c = 0{\cdot}50$ and no adverse effect on pressure recovery is seen. Although the changes appear to be appreciable, it must be remembered that the pressure measurements apply to a very local region of the wing, so that the change in overall drag remains small.

The main reason for the difference in by-pass drag on the side and wing-root intakes is thought to be the unfavourable position of the upper by-pass exits on the side intake, which are too close to the junction between the canopy and the intake fairings; this region is prone to separation even without the added disturbance caused by the efflux, and the interference drag is therefore unnecessarily high, and could easily be avoided without impairing the efficacy of the by-pass by placing the exits on the lower surface of the intake fairing in both designs.

5.3. *Effects of Velocity Ratio, Incidence, and Lip Stagger.* 5.3.1. *Velocity ratio* (V_i/V_0).—All the ducted models were tested at velocity ratios of $0{\cdot}80$, $0{\cdot}65$, and $0{\cdot}50$, values appropriate to high-speed flight. A test was also made on the nose and side intakes with the duct exit faired over giving a velocity ratio of zero. This value, though not representative of a flight condition, is nevertheless of interest partly because it shows up the maximum effect of spillage*, and partly because it is sometimes employed in tests on wind-tunnel models where the construction of ducts inside the model is impracticable.

Neither lift nor pitching-moment characteristics are affected by change of velocity ratio, while the effect on drag varies from model to model and is appreciable only when the duct is closed. Curves of gross drag coefficient against Mach number at velocity ratios of $0{\cdot}65$ and zero are presented in Fig. 23 for the nose and side-intake models while the variation in drag of all three ducted models with velocity ratio is shown directly in Fig. 24. The drag of the nose intake is virtually unaffected by velocity ratio at Mach numbers below $0{\cdot}90$, but above this the drag rises more steeply at $V_i/V_0 = 0$. On the other hand the drag of the side-intake model increases markedly with spillage at all Mach numbers. The increase is small in the range of velocity ratio between $0{\cdot}80$ and $0{\cdot}50$, and occurs mainly between $0{\cdot}50$ and zero velocity ratio.

* By spillage is meant the reduction of velocity ratio below $V_i/V_0 = 1{\cdot}0$.

This difference in behaviour underlines once more the importance of the area ratio of the intake. In potential flow the drag of a ducted body is zero (assuming free-stream pressure to be regained on the parallel portion of the body) whatever the velocity ratio, the thrust force created by spillage over the nose of the body being balanced exactly by the drag associated with the retardation of the internal flow. In practice, viscosity and compressibility both operate to limit the suction values attainable, so that a drag increase may in fact result as the velocity ratio is reduced.

The way in which the thrust over the nose-intake fairing rises as the velocity ratio is reduced is shown by Fig. 25, which gives the pressure distributions at Mach numbers of 0·40 and 0·91 for three sections round the nose at each velocity ratio*. The increase in suction over the nose is slight as the velocity ratio falls from 0·80 to 0·50 but is more pronounced when this is reduced to zero. The low area ratio of the nose intake leaves an appreciable frontal area on which thrust can be developed (0·045 × wing area), but on the side intake this is cut down to 0·01 × wing area, leading to the high levels of suction already noted. Fig. 26 shows that the same qualitative effects with change of velocity ratio are present on this intake as were found on the nose intake; at $M = 0{\cdot}91$, well above the critical Mach number of this intake (*see* Fig. 17), the velocities are supersonic over the greater part of the fairing, the maximum local Mach number being 1·36 when $V_i/V_0 = 0{\cdot}65$, and rising to 1·53 when $V_i/V_0 = 0$.

Values of intake thrust have been derived by integrating the pressure distributions over the outer surfaces of the nose and side-intake fairings for velocity ratios of 0·65 and zero, and these have been plotted in the form of thrust coefficients (referred to wing area) against Mach number in Fig. 27a. The absolute values of these thrust coefficients are not very accurate (as may be seen by comparison with the maximum possible value of thrust predicted by momentum considerations), because the force developed on the inner surfaces of the intake lips has not been taken into account. The critical Mach numbers of the sections at each velocity ratio are indicated on the Figure, and it may be noted how the thrust falls off only after the critical Mach number is exceeded at $V_i/V_0 = 0{\cdot}65$, but on the side intake at zero velocity ratio a serious loss in thrust occurs near $M = 0{\cdot}5$, when viscous effects rapidly reduce the high lip suctions associated with this intake under conditions of high spillage. Fig. 27b compares the increase of thrust due to reduction of the velocity ratio from 0·65 to zero for the nose and side intakes, and it becomes clear that the spillage drag observed in the latter case arises from a deficit in the thrust developed on the intake fairings. By contrast, the nose intake shows no sign of any marked deterioration in performance even at the highest Mach number with zero velocity ratio, again emphasising the value of low area ratio and well-rounded lips.

The effects of velocity ratio on the drag of the wing-root intake are not clearly defined because this model was not tested with the duct sealed, and the changes measured in the range of velocity ratio from 0·80 to 0·50 are small and display no definite trend (Fig. 24). The pressure distributions at sections HH, II and JJ (Fig. 28) show small changes consistent with those already described on the nose and side intakes. Since the effective area ratio is about 50 per cent for the wing-root intake and the lip fairings are therefore relatively sharp, the effect of spillage should be very similar to that obtained on the side intake.

5.3.2. *Incidence.*—Changes of aircraft attitude and velocity ratio are related in that each alters the incidence of the intake lips, and those lip sections which are sensitive to spillage are also the ones more affected by changes of incidence. This is illustrated in Fig. 29 where the quantity $\Delta C_p/\Delta\alpha$† has been plotted against $\sqrt{x}$ for one lip section on each model. In Fig. 29a the loading due to incidence over the mid-section (II, $\eta = 0{\cdot}20$) of the wing-root intake is compared with the chordwise loading measured over the root section (AA, $\eta = 0{\cdot}13$) of the datum model. The presence of the intake increases the loading over the first 10 per cent of the chord at $M = 0{\cdot}40$,

* C_p has been plotted against $\sqrt{x}$ in Figs. 25, 26 and 28 to bring out more clearly the changes in pressure over the forward part of the fairing.

† $\dfrac{\Delta C_p}{\Delta\alpha} \equiv \left[\dfrac{C_p \text{ at } \alpha^\circ - C_p \text{ at } 0^\circ}{\alpha^\circ}\right]_{x,\, M,\, V_i/V_0}$

while at higher Mach numbers the difference, though not so pronounced near the leading edge, extends over a greater fraction of the chord; the difficulty of achieving a satisfactory pressure distribution and of maintaining it at various flight conditions is thus acute. Generally, it appears undesirable to place intakes having sharp lips, which are sensitive to incidence, in the leading edge of the wing because they are there subjected to the large changes in flow direction produced near the stagnation point by the lifting field of the wing.

The effects of incidence on the pressure distribution over section EE of the nose intake and section FF of the side intake are compared in Fig. 29b. The loading over the nose intake is confined largely to the first 10 per cent of the fairing and changes little between M = 0·40 and M = 0·91. The absence of a peak near the lip points the advantage of the thick, well-rounded section, while the fact that the total loading induced over the fairing is smaller than that over the other intakes is due to the low lift slope of the body. The loading over the side-intake fairing is considerably greater and extends over the whole distance covered by the measurements (twice the fairing length). The increase near the front of the fairing is a consequence of the sharper lip shape, while the extension rearwards indicates that the after-part of the fairing lies within the lifting field of the wing.

5.3.3. *Lip stagger.* - Stagger causes the air flowing towards an intake to be deflected towards the lower lip, the deflection increasing as the velocity ratio is reduced. The lips of the nose and wing-root intakes were staggered 15 deg to assist in equalising the velocity distributions over the upper and lower lips at small positive angles of attack; the results achieved are summarised in Fig. 30. The difference between the pressure distributions over the upper and lower lips of the nose intake at α = 0 deg is equivalent to an incidence of about − 1·5 deg both at M = 0·40 and 0·93. On the wing-root intake, however, the velocities over the upper lip are actually higher than those over the lower lip at zero incidence. This may be partly accounted for by the upflow induced at the wing root by the sting, which at an estimated 1 deg (*cf.* Section 4.3) is the same order as the deflection produced by stagger; but it is also probable that the narrow triangular shape and sweepback of this intake reduces the effectiveness of stagger.

6. *Conclusions.*—The effects of different forms of air intake on the longitudinal characteristics of a typical fighter aircraft have been examined at Mach numbers up to 0·93 by testing a series of complete models fitted with nose, side or wing-root intakes and comparing their behaviour with that of a datum model, on which no intake was represented. The type of intake installed is found to have only minor effects on the lift and pitching-moment characteristics (Figs. 7 and 8), but considerable variation in external drag occurs between the different models.

A single intake placed in the nose gives less drag over the whole of the speed range than either form of divided intake (Fig. 9b), the installation of the intake having been achieved without detriment to the design, in spite of the increased frontal area; in fact, the combination of this intake lay-out with shaping of the wing-body junction results in greatly reduced transonic drag. On the side-intake model, the profile drag is increased by about 25 per cent by the operation of the boundary-layer by-passes (Fig. 19), but for which the design would be almost as good as the nose intake as regards external drag up to M = 0·77. Above this Mach number, however, an additional drag rise appears, due to the low critical Mach numbers of the intake fairings (M_{crit} = 0·70) and of the canopy (M_{crit} = 0·8) and to the shock-induced separation which develops in the junction between them (Figs. 15a and 15b). This reduces the drag divergence Mach number to 0·87 compared with 0·89 for the datum model, but at higher Mach numbers the shaping of the fuselage again reduces the steepness of the drag rise (Fig. 9b). On the wing-root-intake model the increased thickness/chord ratio near the root raises the profile drag by about 20 per cent, but no reduction in drag divergence Mach number occurs. Above M = 0·9, however, the drag rises more steeply than that of the other intake models showing that the increase in sweepback built into the wing-root is less effective than the shaping of the wing-body junction in reducing the transonic drag of the aircraft. In this design the boundary-layer by-pass causes only a small increase in drag (Fig. 21b).

The results bear out the importance of the area ratio of an intake, and the nose intake owes much of its superiority over the divided intakes to its lower area ratio (18 per cent compared with 55 per cent for the side intakes and a mean value of 50 per cent for the wing-root intakes). This allows a well-rounded lip shape to be combined with a fairing of high fineness ratio (approximately 7) giving a high critical Mach number (0·86) and minimising the adverse effects of spillage and of incidence. The high area ratios of the side and wing-root intakes, however, lead to lip fairings which have much lower critical Mach numbers (Fig. 17), and which are much more sensitive to flow conditions. In addition, the smaller frontal area of the fairings limits the thrust they can develop, although this is only apparent under extreme conditions within the range of Mach number of these tests ($V_i/V_0 = 0$, Fig. 23). At moderate supersonic speeds, however, the total thrust available from these two designs may be penalised, at a given velocity ratio, at a lower Mach number than in the case of the nose intake. In general, the intake design procedure (outlined in Section 2.2) has proved to be reasonable.

The high drag set up by the side-intake boundary-layer by-pass compared with that from the wing-root intake by-pass is due to the excessive interference set up by the efflux in the canopy-intake junction; the obvious remedy is to discharge the whole of the by-passed flow through exits sited underneath the intakes.

Many of the criticisms of the side-intake lay-out could be met by moving the intakes forward towards the nose. This would at once reduce the depth of the boundary layer to be bled off and lessen the interference between the canopy and the intakes. Some improvement in area ratio should also result as the intakes come closer together, while finally the intakes would be further removed from the wings. This type of intake is therefore considered to be potentially better than the wing-root intake, which (at least on fighter aircraft), is clearly the most difficult to perfect.

LIST OF SYMBOLS AND DEFINITIONS

H	Free-stream total head
Area ratio	Minimum cross-sectional area of the intake duct (*i.e.*, throat area) ÷ maximum cross-sectional area of the intake housing
Velocity ratio V_i/V_0	Mean inlet velocity at intake throat ÷ speed of aircraft
Position ratio S/A	Surface area of fuselage wetted by air flowing into intake ÷ intake throat area (Ref. 1)
L	Length of intake fairing
T	Thickness of intake lip
t	Thickness of inner lip-fairing (*see* Fig. 5)
η	Distance outboard of centre-line as fraction of semi-span

REFERENCES

No.	*Author*	*Title, etc.*
1	J. Seddon	Air intakes for aircraft gas turbines. *J. R. Ae. Soc.* Vol. 56. No. 502. pp. 747 to 781. October, 1952.
2	D. E. Hartley	Investigation at high subsonic speeds of wing-fuselage intersection shapes for swept-back wings. Part I. R.A.E. Report Aero. 2464. A.R.C. 15,165. May, 1952. Part II. R.A.E. Report Aero. 2503. A.R.C. 16,780. December, 1953.
3	D. A. Kirby and W. J. G. Trebble	Low-speed tunnel measurements of the drag of the *Supermarine Swift* (F105P). R.A.E. Tech. Note Aero. 2194. November, 1952.
4	D. Küchemann and J. Weber	*Aerodynamics of Propulsion.* McGraw-Hill Book Company. 1952.
5	D. D. Baals, N. F. Smith, and J. B. Wright	The development and application of high-critical-speed nose inlets. N.A.C.A. Report 920. 1949.
6	C. R. Bryan and F. F. Fleming	Some internal flow characteristics of several axisymmetric N.A.C.A. 1-series nose air inlets at zero flight speed. N.A.C.A. Research Memo. L54E19a, TIL 4295. July, 1954.
7	D. Küchemann	Design of wing junction, fuselage and nacelles to obtain the full benefit of swept-back wings at high Mach number. R.A.E. Report Aero. 2219. A.R.C. 11035. August, 1947.
8	J. Seddon and W. J. G. Trebble	Experiments on the flow into a swept leading-edge intake at zero forward speed with notes on the wider uses of a slotted intake. R. & M. 2909. January, 1951.
9	J. Y. G. Evans	Corrections to velocity for wall constraint in any 10 × 7 rectangular subsonic tunnel. R. & M. 2662. April, 1949.
10	D. Küchemann	A simple method for calculating the span and chordwise loadings on thin swept wings. R.A.E. Report Aero. 2392. A.R.C. 13,758. August, 1950.
11	D. Küchemann and J. Weber	The subsonic flow past swept wings at zero lift without and with body. R. & M. 2908. March, 1953.
12	H. H. Pearcey	Some effects of shock-induced separation of turbulent boundary layers in transonic flow past aerofoils. A.R.C. 17,681. June, 1955.
13	W. J. G. Trebble and R. Fail ..	An investigation into the pressure distribution on aircraft cabins. R.A.E. Tech. Note Aero. 2149. A.R.C. 15,038. February, 1952.
14	—	Report of the definitions panel on the definitions of the thrust of a jet engine and of the internal drag of a ducted body. C.P. 190. May, 1954.

APPENDIX I

Measurement of internal drag

The internal drag of the ducts was derived from measurements of pitot and static pressures taken in the exit plane using an extension of Jones's method; one of the rakes used is illustrated in Fig. 6a. The value thus obtained has been defined as the Jones internal drag by the definitions panel of the A.R.C.[14] and is denoted by C_{DJ} (Fig. 10), where

$$C_{DJ} \equiv \frac{\text{Internal Drag}}{\frac{1}{2}\rho_0 V_0^2 S}.$$

Let suffix $_0$ refer to free-stream conditions,
suffix $_1$ refer to flow conditions in the entry plane,
suffix $_2$ refer to flow conditions in the exit plane,
suffix $_3$ refer to flow conditions in a plane far downstream.

The internal drag of the duct is equal to the loss of momentum between the two stations 0 and 3, *i.e.*,

$$D_J = \int \rho_3 V_3 (V_0 - V_3)\, dA_3 ,$$

where A_3 is the cross-sectional area of the internal flow in the plane 3.

By continuity,

$$D_J = \oint \rho_2 V_2 (V_0 - V_3)\, dA_2 ,$$

where $\oint$ is taken over the duct exit.

Therefore
$$C_{DJ} = \frac{2}{S} \oint \frac{\frac{1}{2}\rho_2 V_2^2}{\frac{1}{2}\rho_0 V_0^2} \left(\frac{V_0}{V_2}\right) \left[1 - \frac{V_3}{V_0}\right] dA_2 .$$

Making the assumption that the pressure recovery between planes 2 and 3 takes place isentropically and without mixing, and that the static pressure has regained its free-stream value at plane 3, then

$$H_2 = H_3 \quad \text{and} \quad p_3 = p_0, \text{ giving}$$

$$C_{DJ} = \frac{2}{S} \oint \frac{p_2}{p_0} \left[\frac{\left(\frac{p_2}{H_2}\right)^{(1-\gamma)/\gamma} - 1}{\left(\frac{p_0}{H_0}\right)^{(1-\gamma)/\gamma} - 1}\right] \left\{\frac{\left[1 - \left(\frac{p_0}{H_0}\right)^{(\gamma-1)/\gamma}\right]}{\left[1 - \left(\frac{p_2}{H_2}\right)^{(\gamma-1)/\gamma}\right]}\right\}^{1/2} \left[1 - \left\{\frac{1 - \left(\frac{p_0}{H_2}\right)^{(\gamma-1)/\gamma}}{1 - \left(\frac{p_0}{H_0}\right)^{(\gamma-1)/\gamma}}\right\}^{1/2}\right] dA_2 ,$$

which may be expressed in the form

$$C_{DJ} = \frac{1}{S} \int f_2 \times f_{02}\, dA_2 ,$$

where

$$f_2 = \left(\frac{p_2}{H_2}\right)^{1/\gamma} \left[1 - \left(\frac{p_2}{H_2}\right)^{(\gamma-1)/\gamma}\right]^{1/2},$$

and

$$f_{02} = 2\left(\frac{p_0}{H_2}\right)^{-1} \left[\left(\frac{p_0}{H_0}\right)^{(1-\gamma)/\gamma} - 1\right]^{-1} \left[\left\{1 - \left(\frac{p_0}{H_0}\right)^{(\gamma-1)/\gamma}\right\}^{1/2} - \left\{1 - \left(\frac{p_0}{H_2}\right)^{(\gamma-1)/\gamma}\right\}^{1/2}\right].$$

The seventeen pitot-tubes were spaced so as to cover equal areas of the duct exit, so that

$$C_{DJ} = \frac{A_2}{S} \sum_1^{17} (f_2 f_{02}) .$$

To simplify the evaluation of the internal drag, charts showing the values of f_2 and f_{02} over the required range of Mach number and (p_0/H_2) were prepared beforehand.

TABLE 5

Leading Dimensions of Models

Wing

Gross area	374·56 sq in.
Span	34·34 in.
Standard mean chord	10·91 in.
Aspect ratio	3·15
Taper ratio	0·378
Aerofoil section	Thwaites 9 per cent
Position of maximum thickness	$0{\cdot}38c$
Sweepback of $\frac{1}{4}$-chord line	38·45°
Distance of mean $\frac{1}{4}$-chord point aft of wing leading-edge vertex	9·76 in.
Pitching-moment reference axis	$0{\cdot}295\bar{c}$

Intakes

Total intake area (excluding by-pass area for side and wing-root intakes)	3·784 sq in.
Duct exit area for $V_i/V_0 = 0{\cdot}50$	2·570 sq in.
Duct exit area for $V_i/V_0 = 0{\cdot}65$	3·142 sq in.
Duct exit area for $V_i/V_0 = 0{\cdot}80$	3·597 sq in.
Total by-pass area for side intake	0·636 sq in.
Total by-pass area for wing-root intake	0·474 sq in.

Fuselage

Intake:		Datum	Nose	Side	Wing root
Maximum cross-sectional area	(sq in.)	+15·06	+21·40	+21·40	+15·06
Maximum width	(in.)	4·38	6·22	6·22	4·38
Maximum height	(in.)	4·38	4·38	4·38	+ 4·38
Distance forward of wing leading-edge vertex of:					
Plane of intake throat	(in.)	—	7·18	0·33	− 4·54
Nose	(in.)	+ 8·64	+ 7·75	+ 8·64	+ 8·64
Rear end of body (zero flow)	(in.)	−35·76	−37·35	−37·35	−38·83

TABLE 6

Wing-section Co-ordinates for all Models

x/c (per cent)	z/c (per cent)	x/c (per cent)	z/c (per cent)
0	0	40	4·50
0·5	0·86	45	4·43
1	1·16	50	4·29
2	1·57	55	4·06
5	2·32	60	3·76
7·5	2·75	65	3·39
10	3·11	70	2·97
12·5	3·39	75	2·49
15	3·63	80	2·01
17·5	3·83	85	1·51
20	3·99	90	1·01
25	4·24	95	0·51
30	4·41	100	0
35	4·50	Leading-edge radius (per cent chord)	0·81

Maximum thickness at 38 per cent chord

TABLE 7

Proportions and Lengths of the Lip Sections of the Three Intakes

(*See* Figs. 4 and 5 for the section positions and the definition of L, T and t)

Intake	Section	L/T	t/T	L (in.)
Nose Intake ..	CC	6·15	0·111	10·071
Nose Intake ..	DD	7·23	0·073	9·874
Nose Intake ..	EE	7·05	0·073	9·626
Side Intake ..	FF	2·87	0·067	1·490
Side Intake ..	GG	3·79	0·089	1·490
Wing-root Intake	HH	2·55	0·094	1·224
Wing-root Intake	II	4·08	0·081	2·264
Wing-root Intake	JJ	5·25	0·072	3·304

TABLE 8

Windwise Section across the Wing-root Intake at $\eta = 0{\cdot}177$

Fairing between intake and the maximum thickness position: quarter-ellipse, forming intake lip: $T = 0{\cdot}472$ in.; $t = 0{\cdot}045$ in.; $L = 1{\cdot}745$ in. (upper surface), $1{\cdot}755$ in. (lower surface).

Fairing between maximum-thickness position and trailing edge :

x/X	Z/Z_{max}	x/X	Z/Z_{max}
0	1·0	0·6	0·5157
0·1	0·9724	0·7	0·3908
0·2	0·9134	0·8	0·2628
0·3	0·8352	0·9	0·1318
0·4	0·7418	1·0	0
0·5	0·6352		

where Z = local thickness ordinate, $Z_{max} = 1{\cdot}060$ in.

X = length of rear fairing,

= $11{\cdot}507$ in. (upper surface), $11{\cdot}182$ in. (lower surface).

TABLE 9

Co-ordinates for Waisted Body of Side and Nose-Intake Models

$\frac{x}{c}$	Body width / Waist diameter	$\frac{x}{c}$	Body width / Waist diameter
−0·200	1·24	0·600	1·04
−0·150	1·31	0·650	1·01
−0·100	1·37	0·700	1·00
−0·050	1·40	0·750	1·00
0	1·42	0·800	1·01
+0·050	1·42	0·850	1·03
0·100	1·40	0·900	1·05
0·150	1·38	0·950	1·08
0·200	1·35	1·000	1·11
0·250	1·32	1·050	1·15
0·300	1·28	1·100	1·19
0·350	1·24	1·150	1·23
0·400	1·19	1·200	1·26
0·450	1·16		
0·500	1·12		
+0·550	1·08		

where c is the wing chord at the intersection of the wing and the cylinder, co-axial with the body, whose diameter equals the waist diameter of the body,

x is measured rearward from the leading-edge point at this intersection.

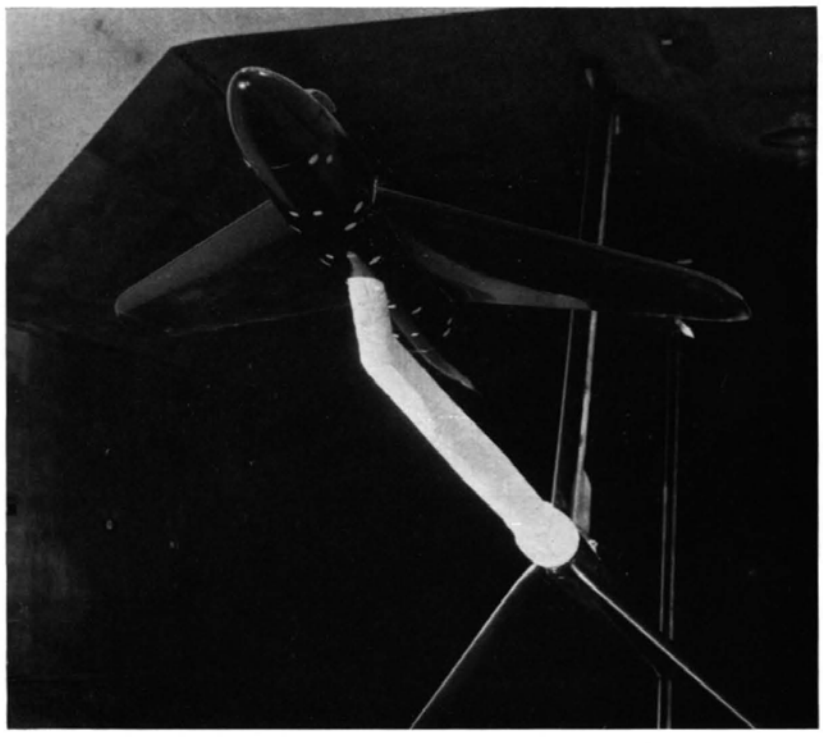

FIG. 1a. The datum model.

FIG. 1b. The wing-root intake model.

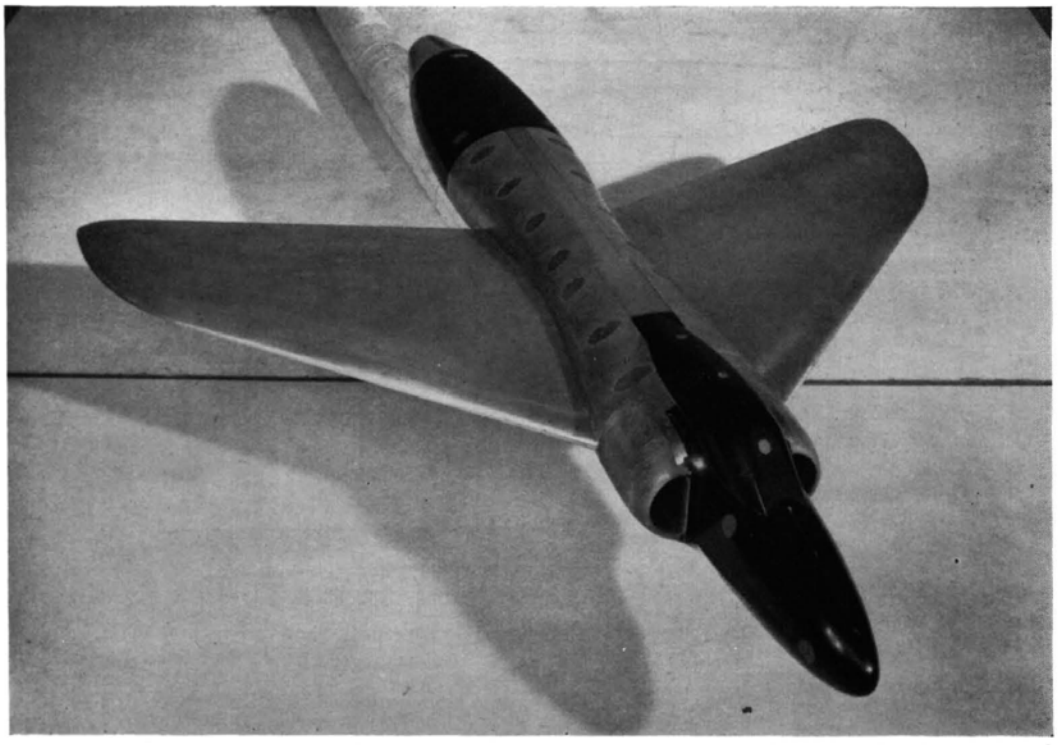

FIG. 1c. The side-intake model.

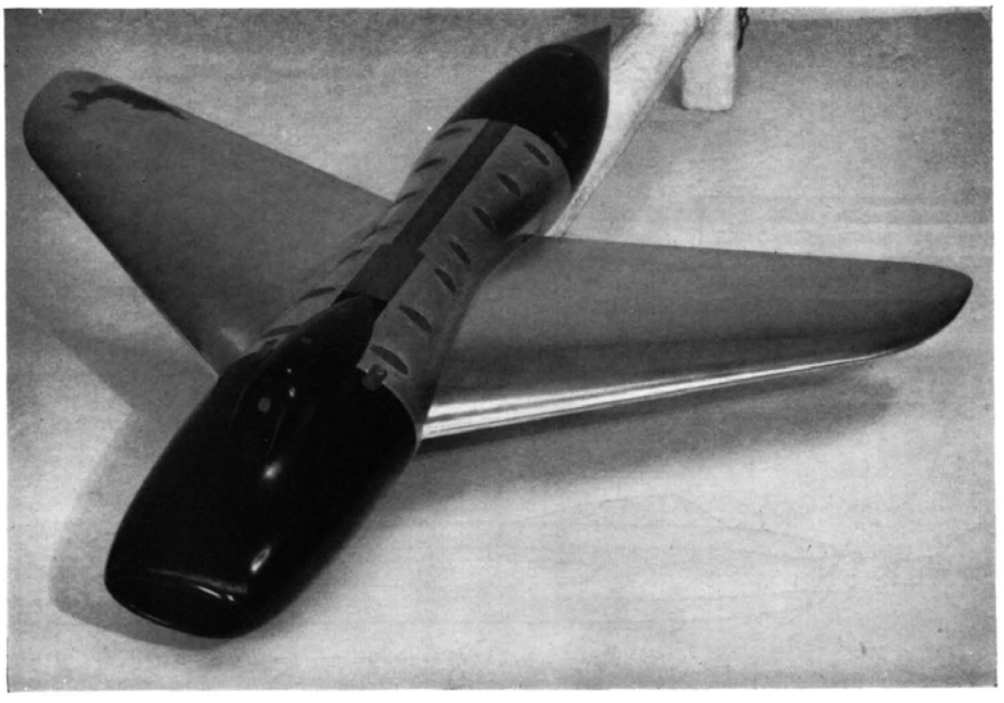

FIG. 1d. The nose-intake model.

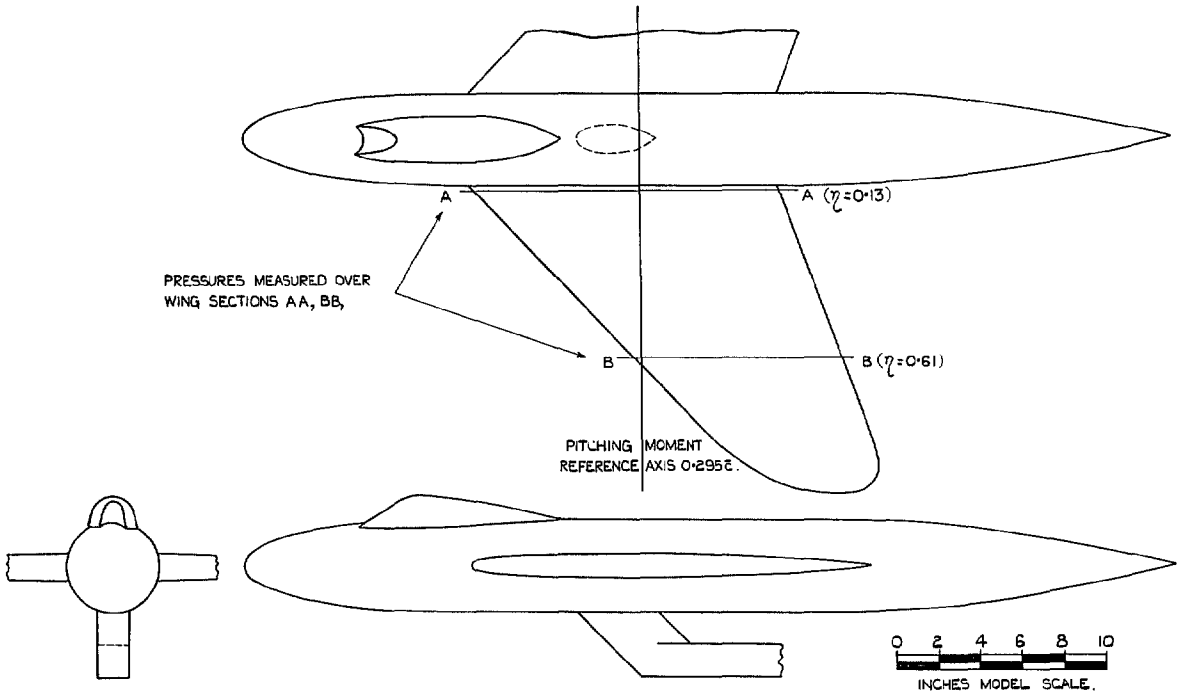

FIG. 2a. General arrangement of datum model.

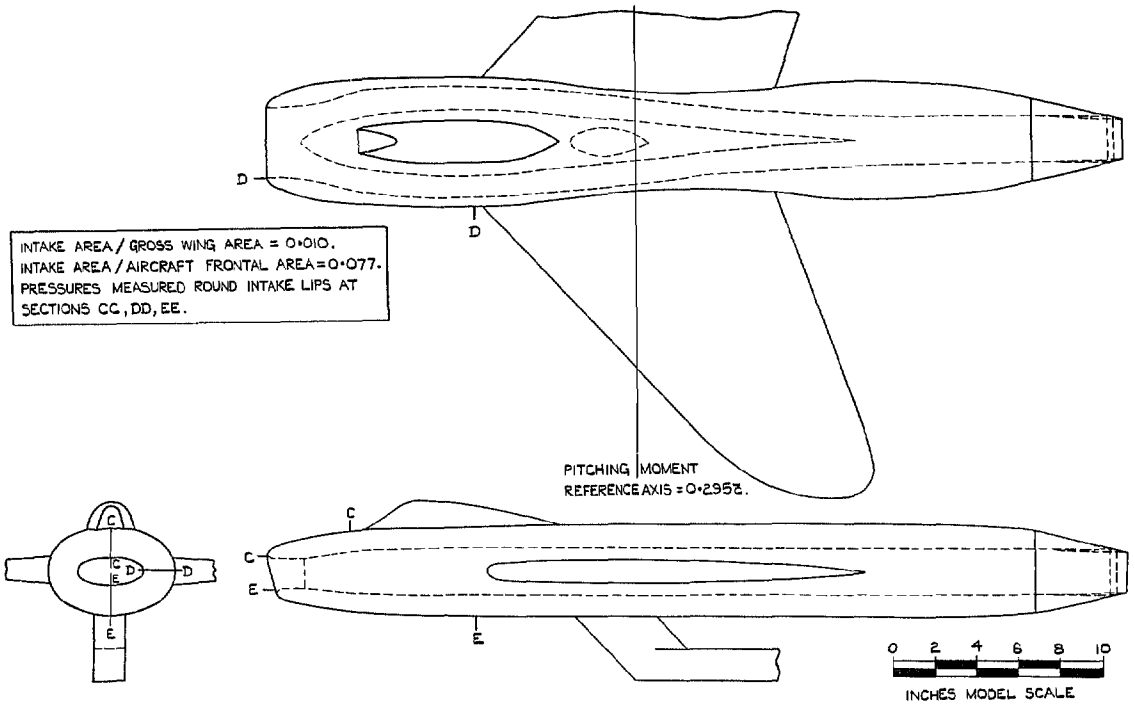

FIG. 2b. General arrangement of nose-intake model.

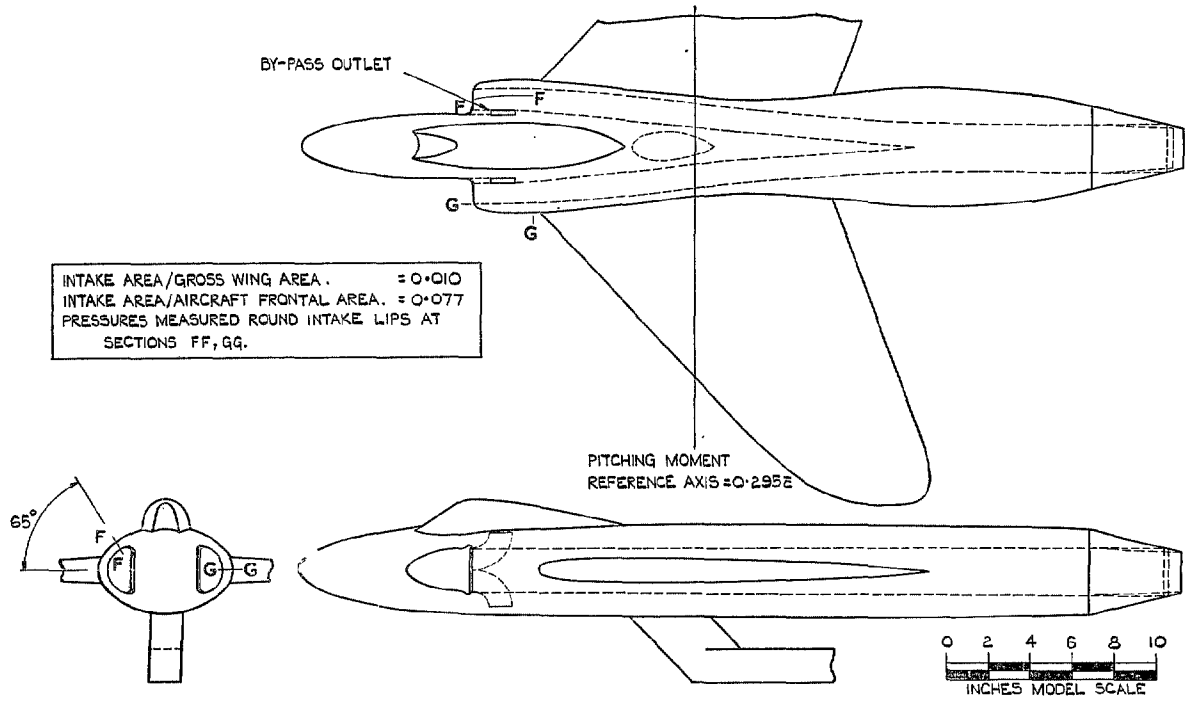

FIG. 2c. General arrangement of side-intake model.

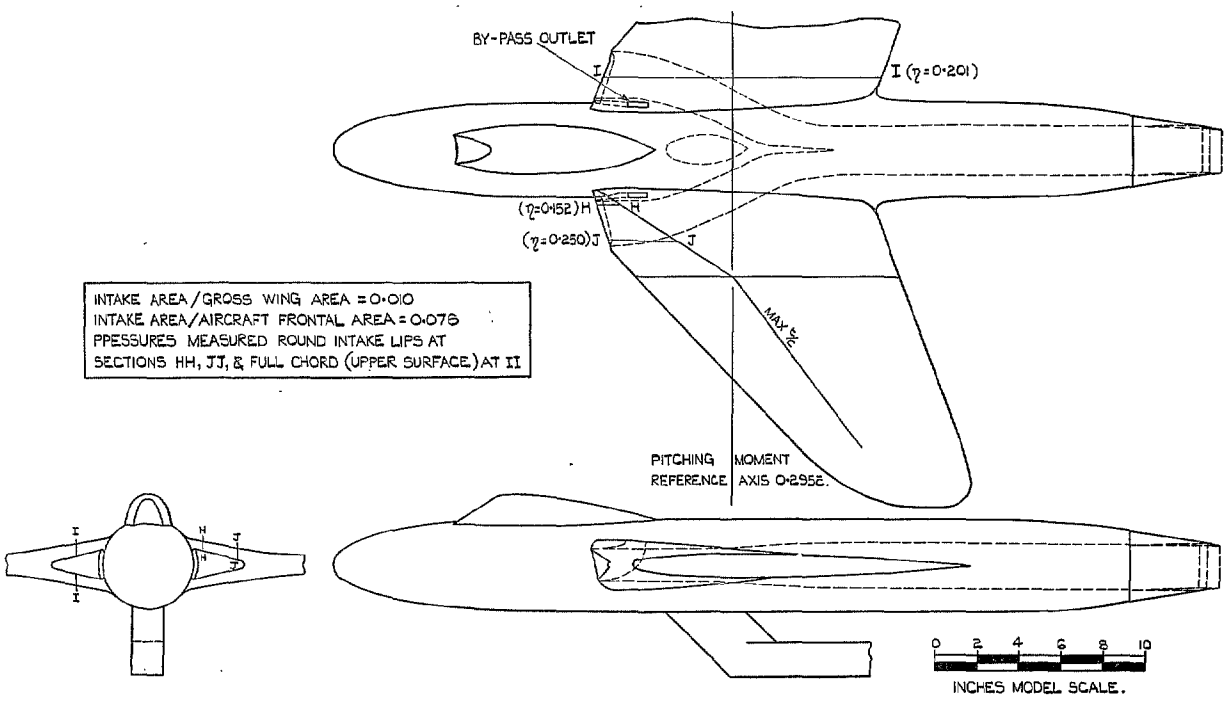

FIG. 2d. General arrangement of wing-root intake model.

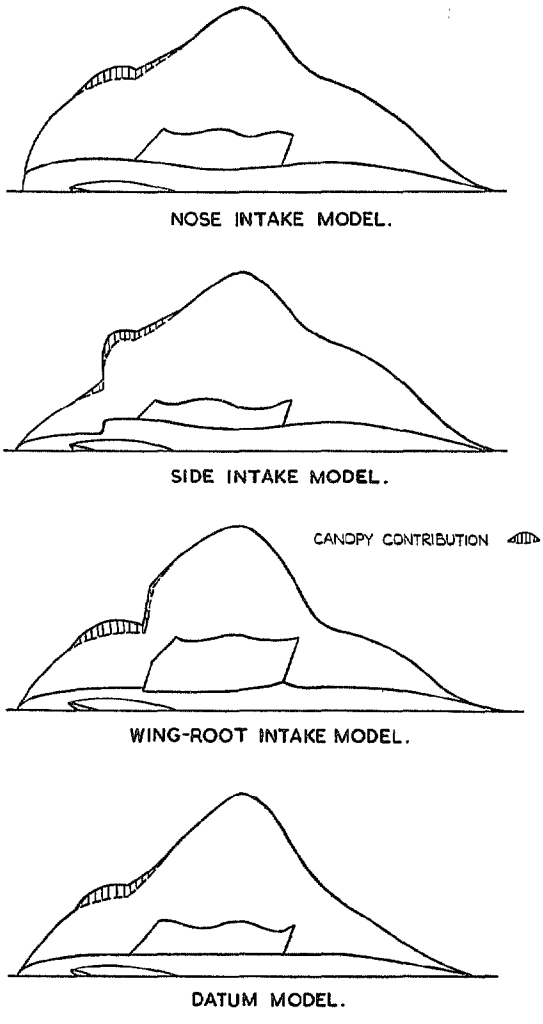

FIG. 3. Axial variation of cross-sectional area of the different intake models.

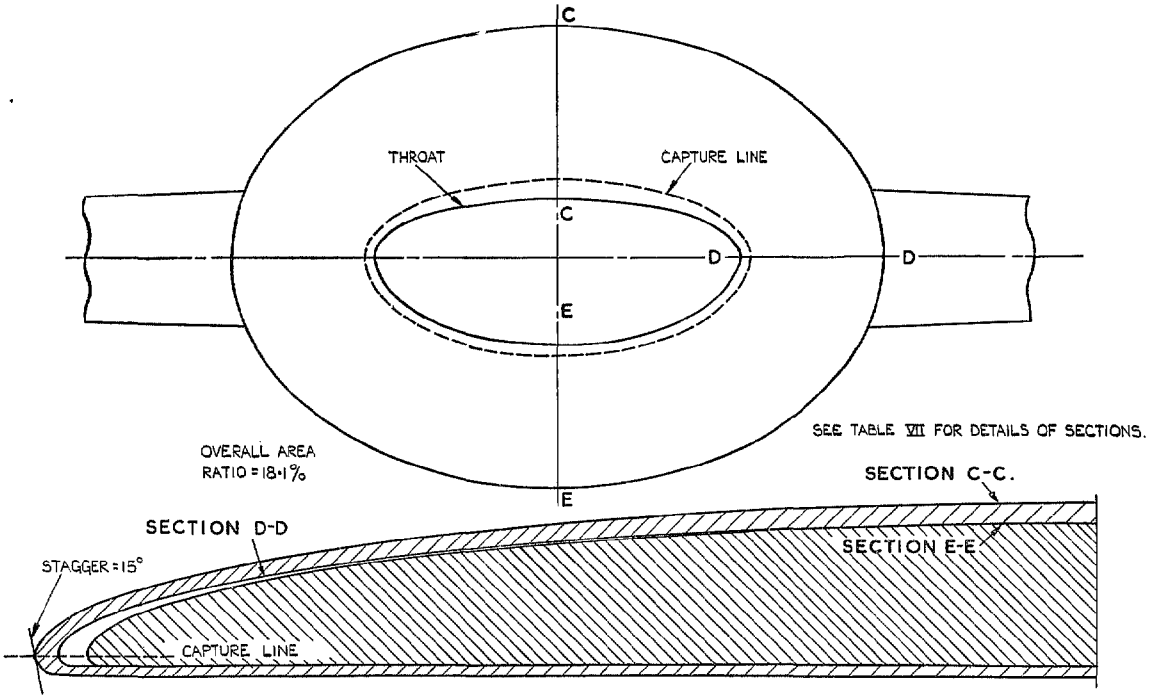

FIG. 4a. Detail of the intake lay-out of the nose-intake model.

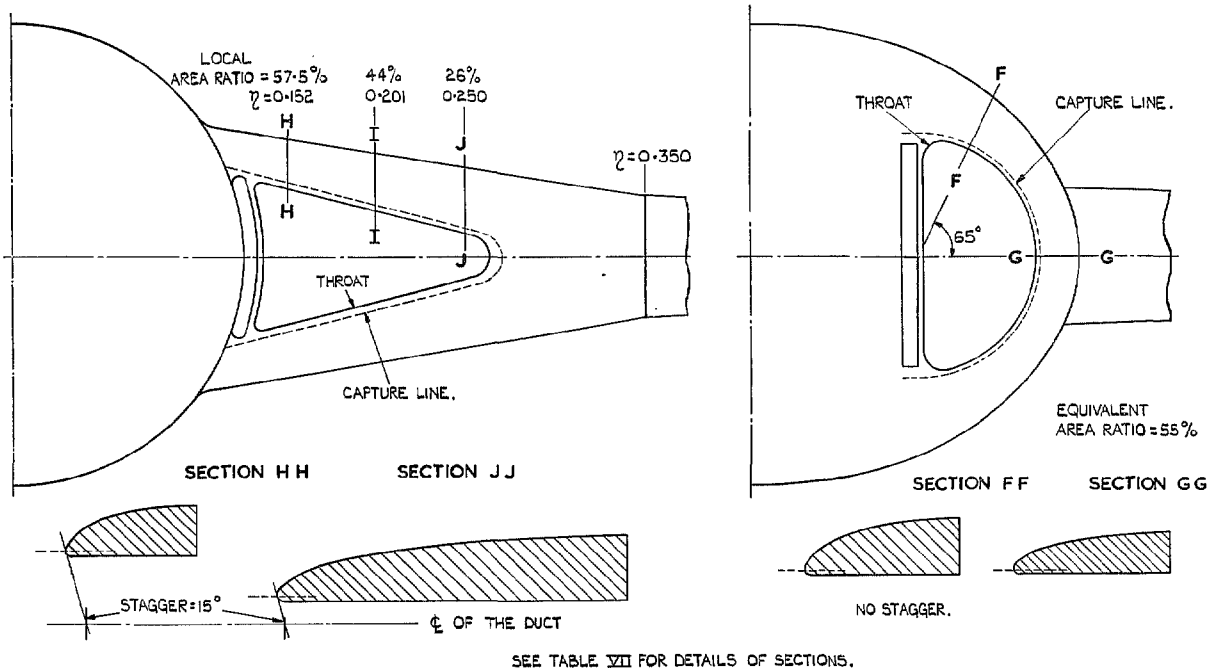

FIG. 4b. Details of the intake lay-outs of the wing-root and side-intake models.

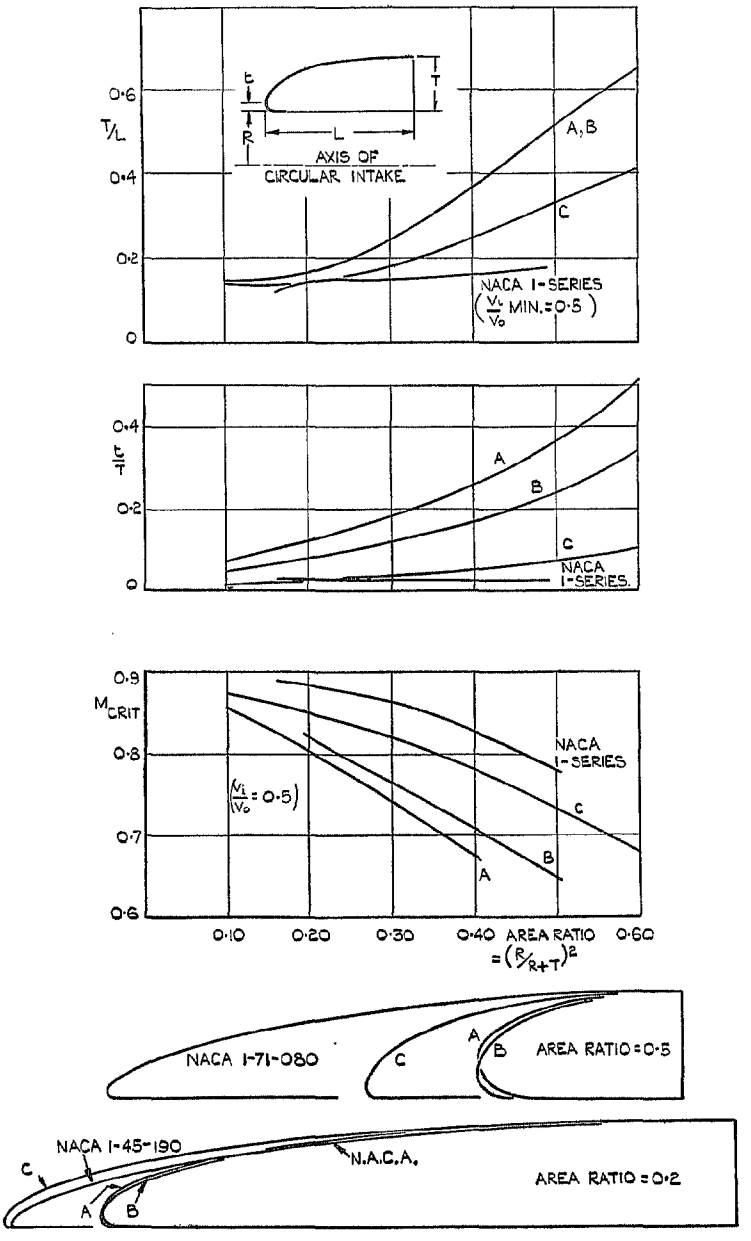

FIG. 5. Comparison of the properties of the N.A.C.A. 1-Series and Küchemann class A, B and C lip fairings.

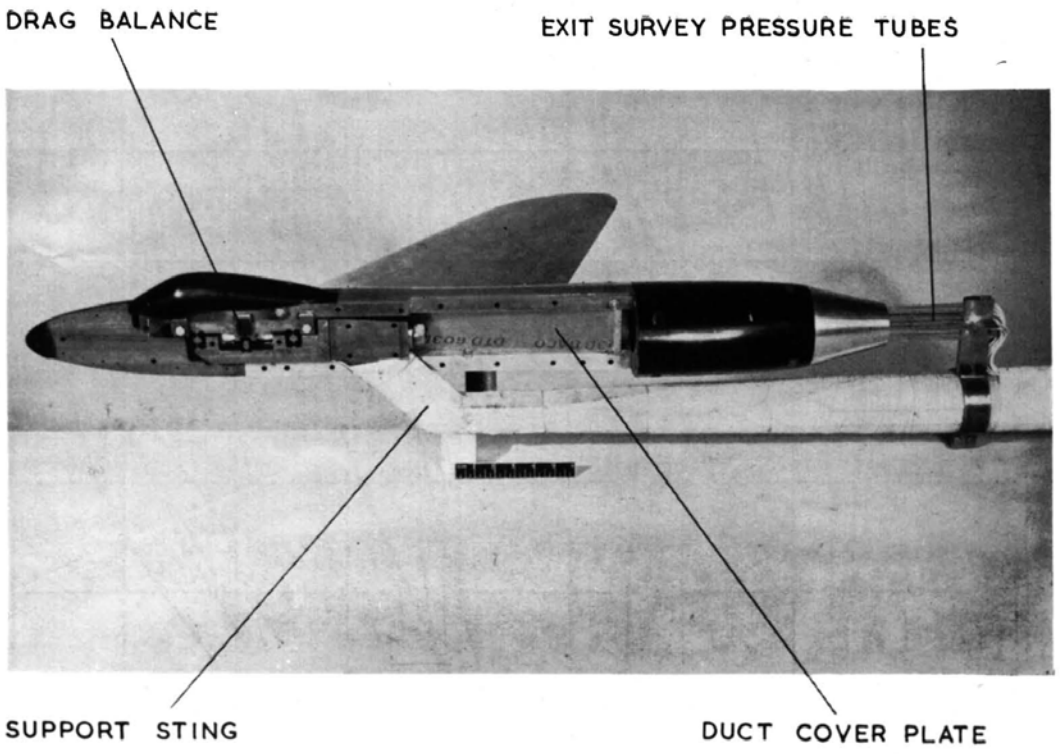

FIG. 6a. Interior view of side intake model.

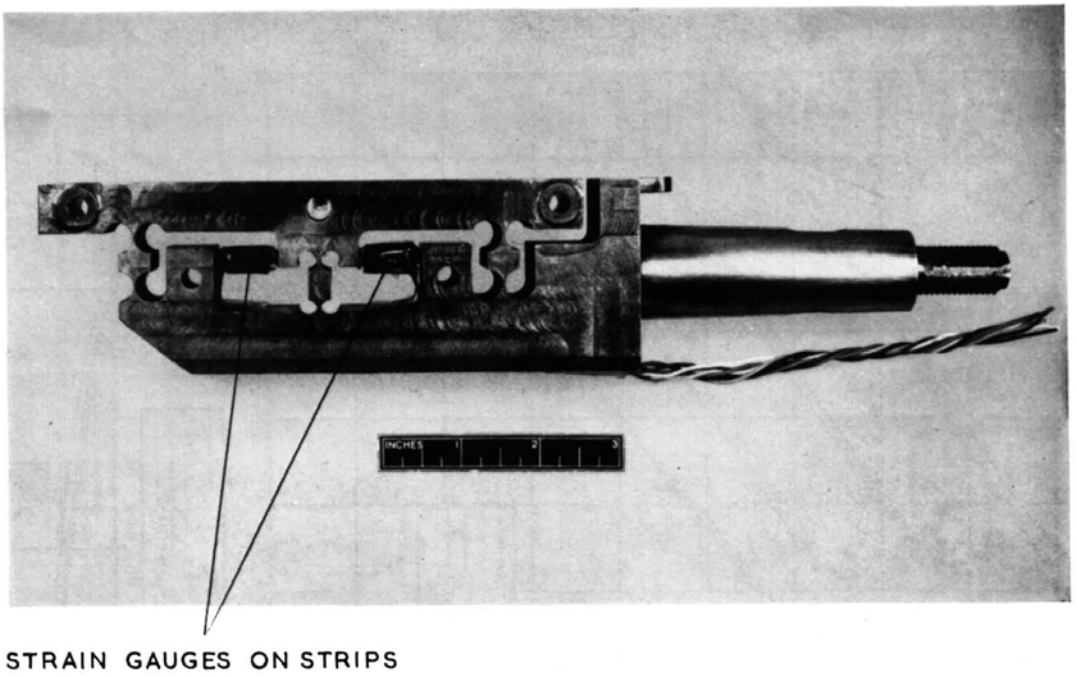

FIG. 6b. The strain-gauge ' drag balance '.

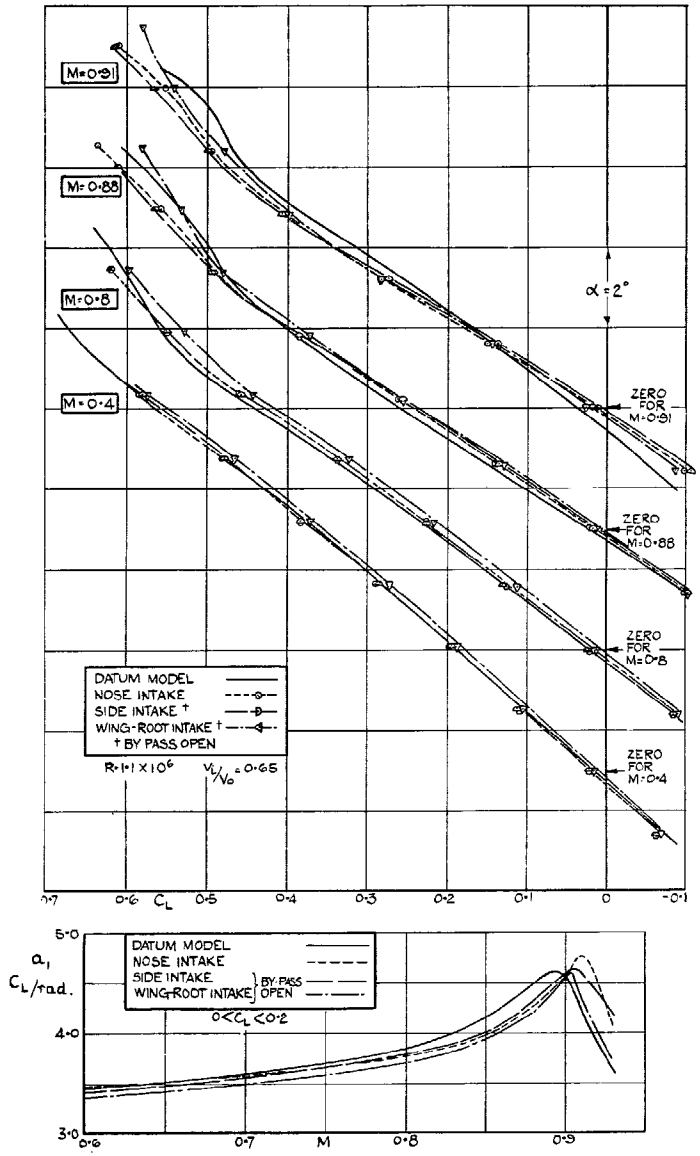

FIG. 7. C_L *vs.* α at constant Mach number, and lift slope *vs.* Mach number. Comparison between the different intake designs.

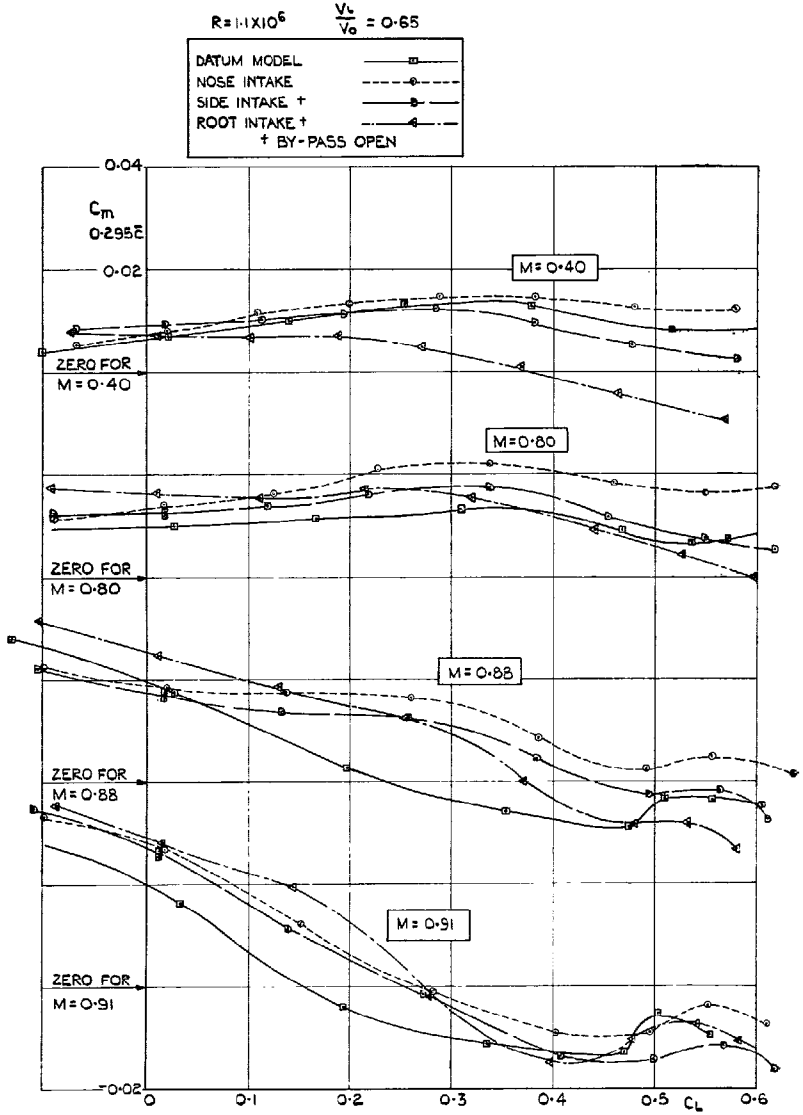

FIG. 8. C_m *vs.* C_L at constant Mach number. Comparison between the different intake designs.

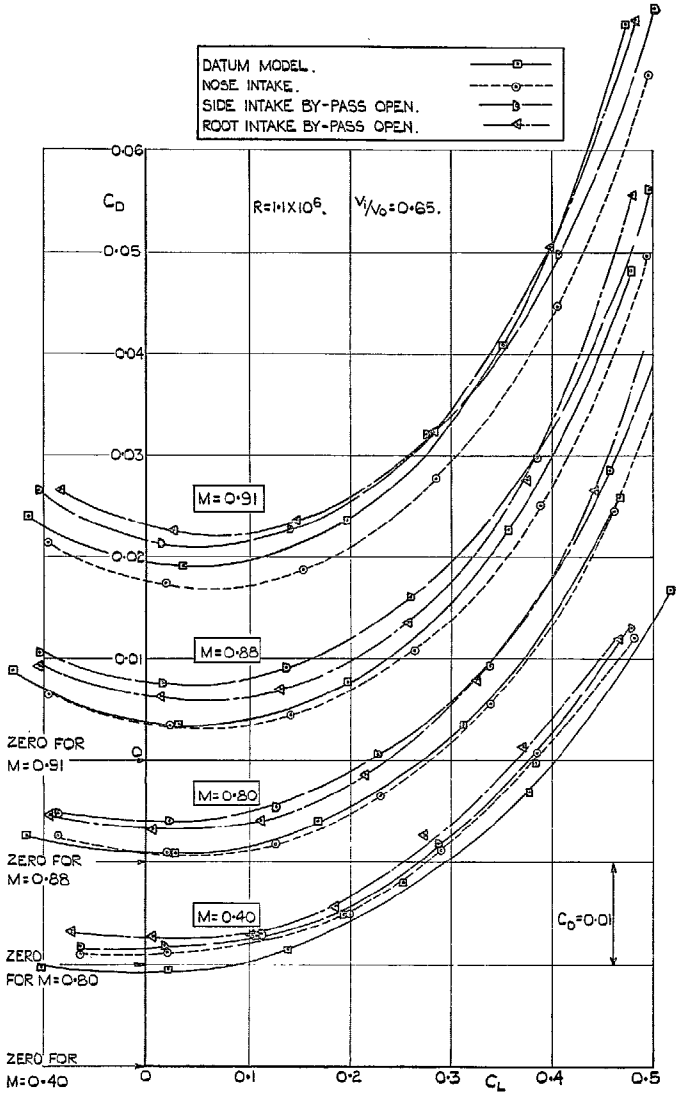

FIG. 9a. Gross C_D *vs.* C_L at constant Mach number. Comparison between the different intake designs.

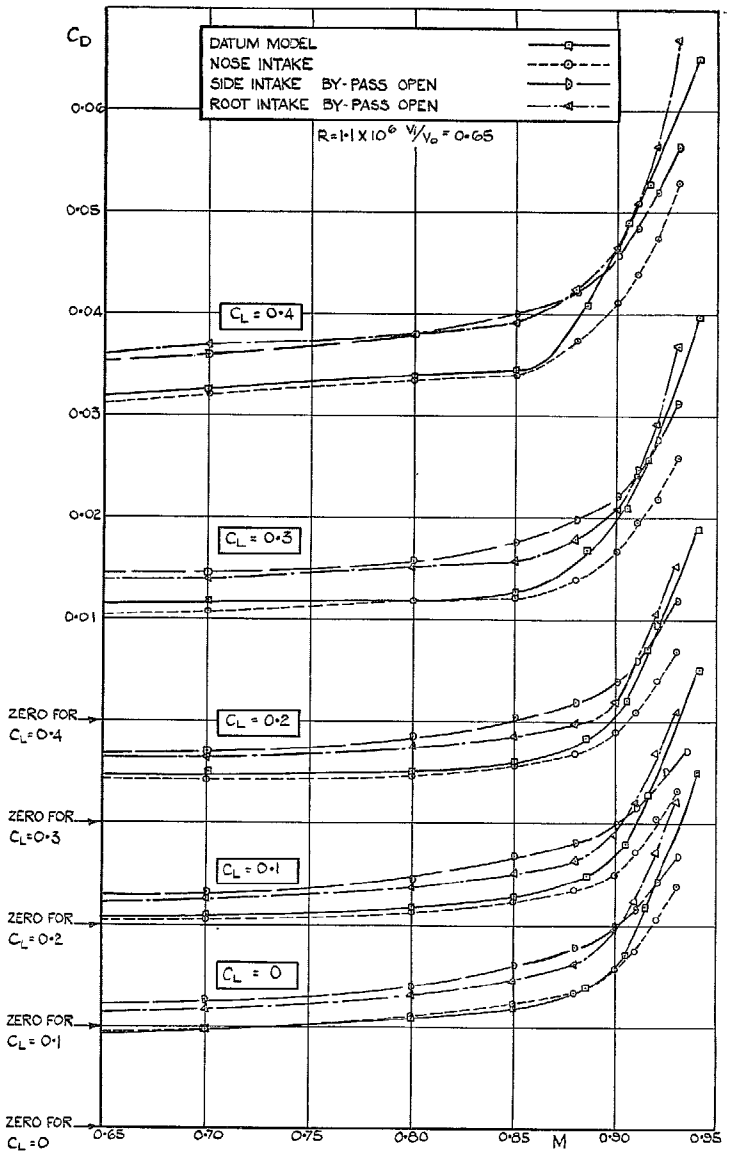

FIG. 9b. Gross C_D *vs.* Mach number at constant C_L. Comparison between the different intake designs.

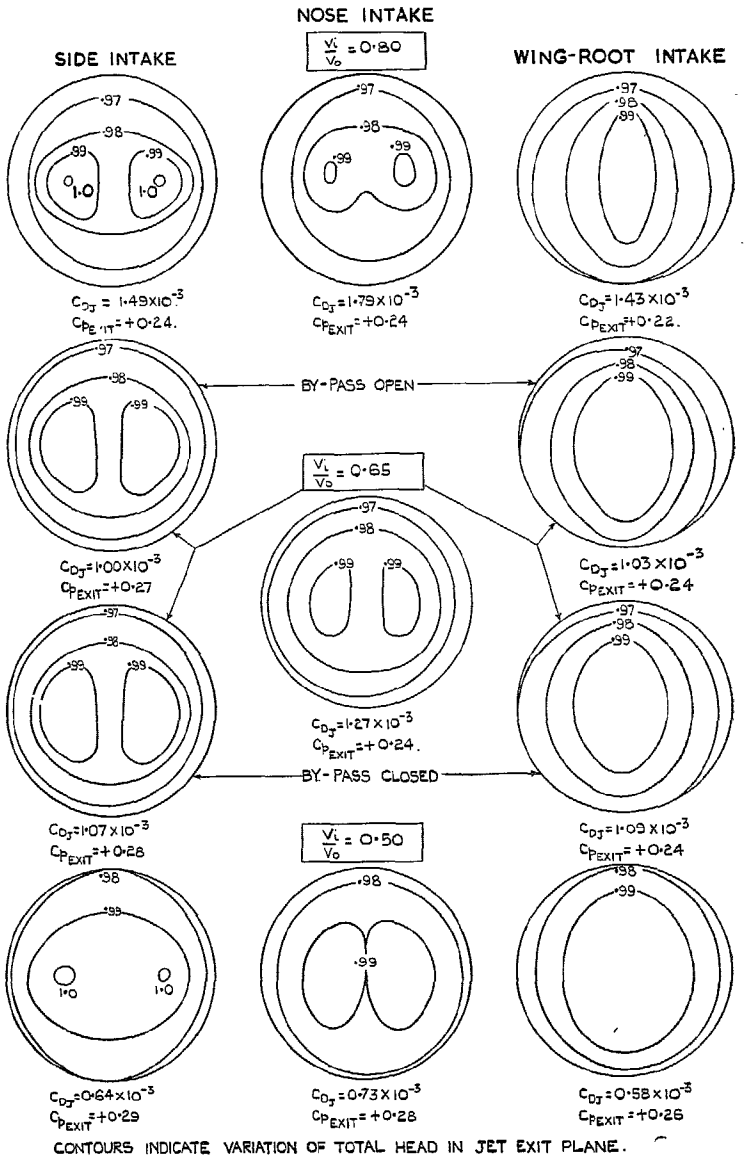

FIG. 10a. Internal drag coefficient at $M = 0{\cdot}40$, $\alpha = 0$ deg. Comparison between the different intake designs.

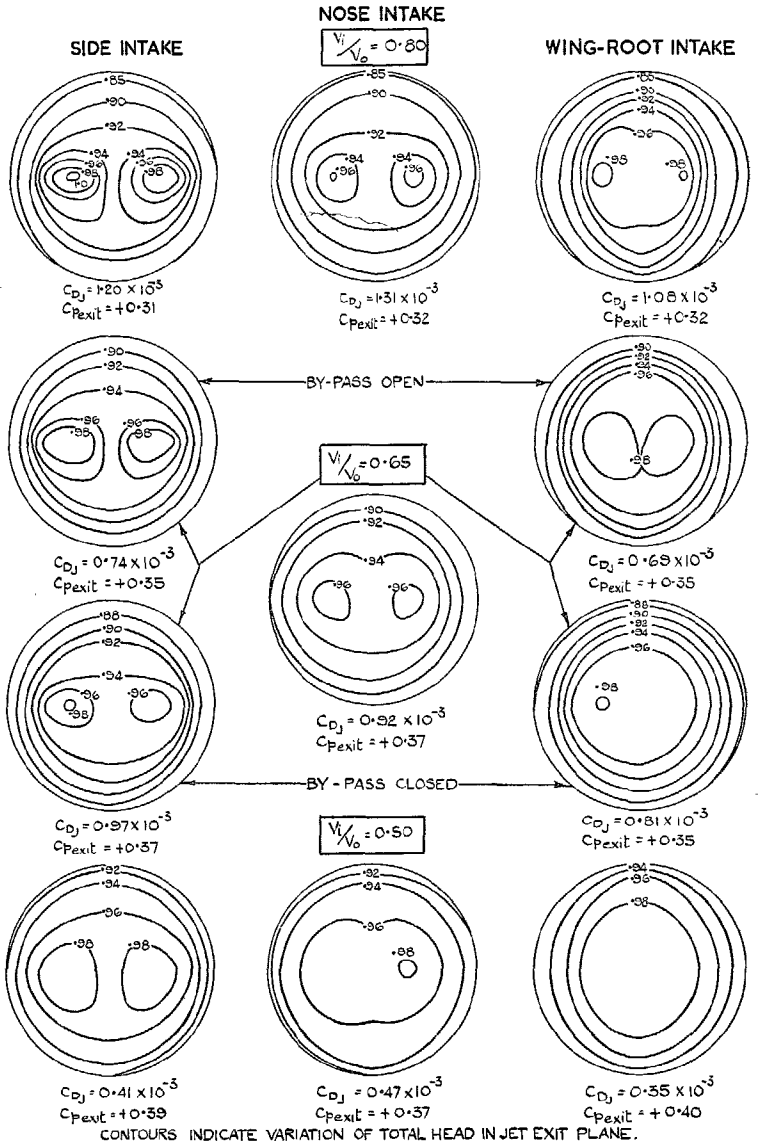

FIG. 10b. Internal drag coefficient at $M = 0{\cdot}93$, $\alpha = 0$ deg. Comparison between the different intake designs.

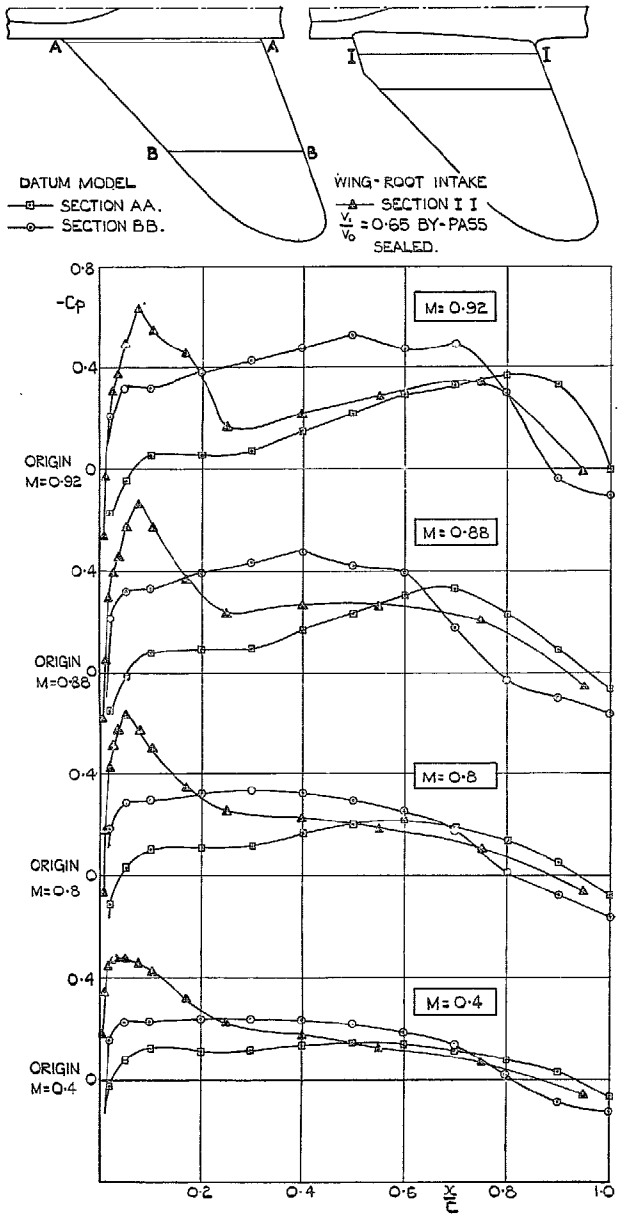

FIG. 11a. Comparison between the pressure distributions at $\alpha = 0$ deg on the datum model wing and the wing-root intake.

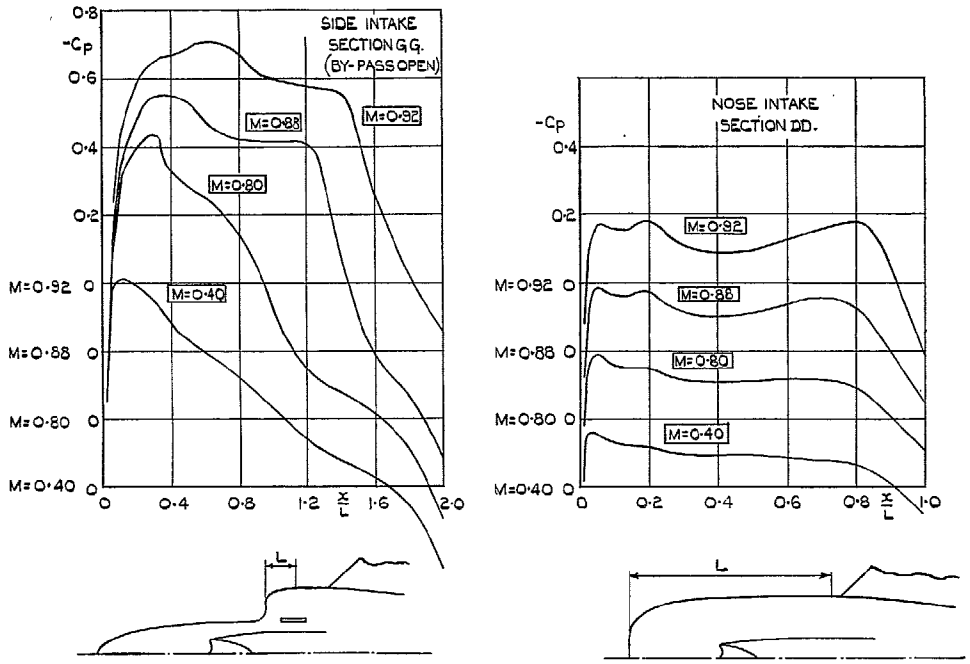

FIG. 11b. Comparison between the pressure distributions at $\alpha = 0$ deg on the side and nose-intake lip fairings ($V_i/V_0 = 0{\cdot}65$).

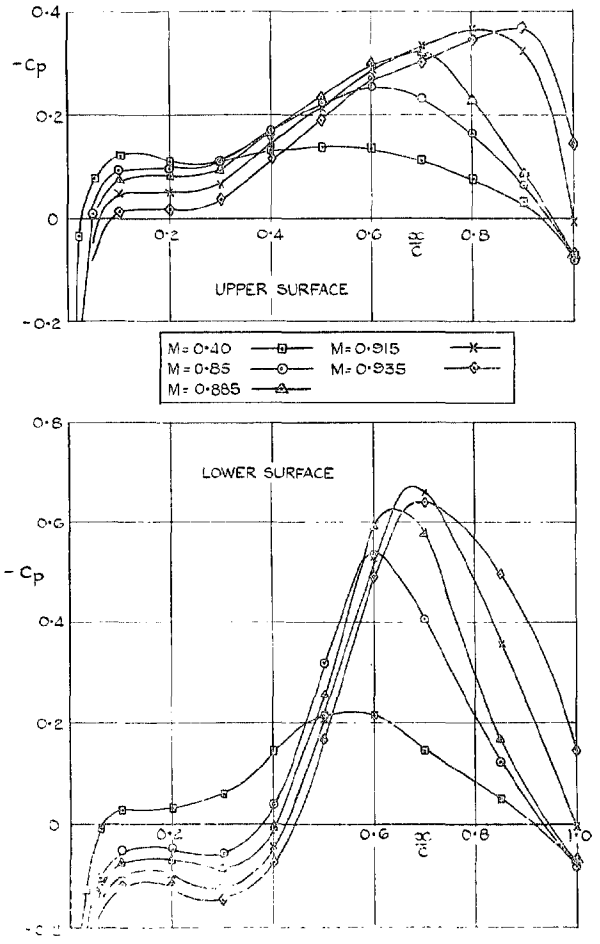

FIG. 12a. Effect of Mach number on the pressure distributions over the wing of the datum model. Section AA (η 0·13) at $\alpha = 0$ deg.

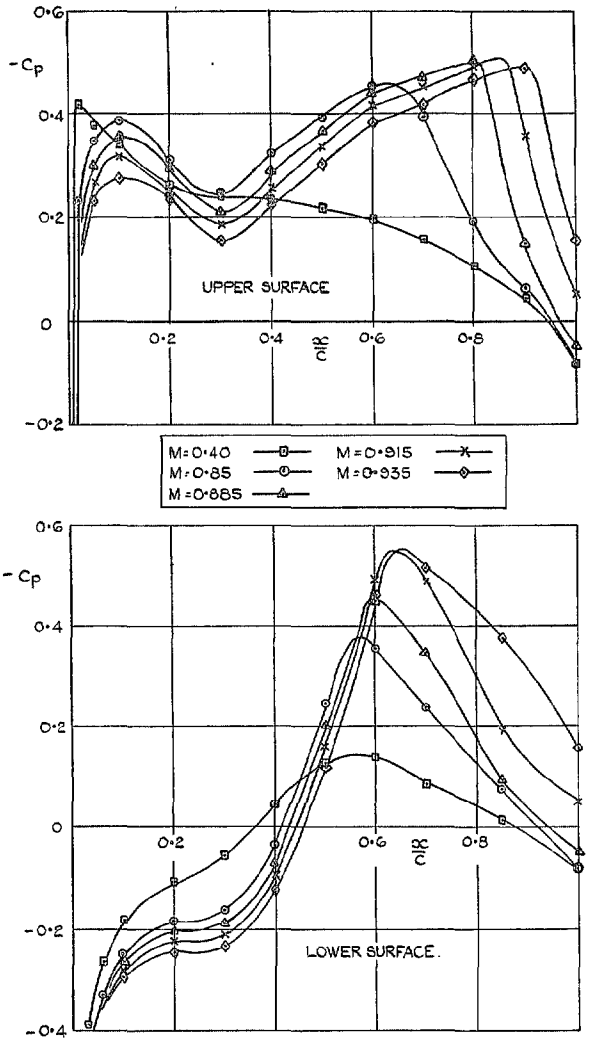

FIG. 12b. Effect of Mach number on the pressure distributions over the wing of the datum model. Section AA ($\eta = 0 \cdot 13$) at $\alpha = 4$ deg.

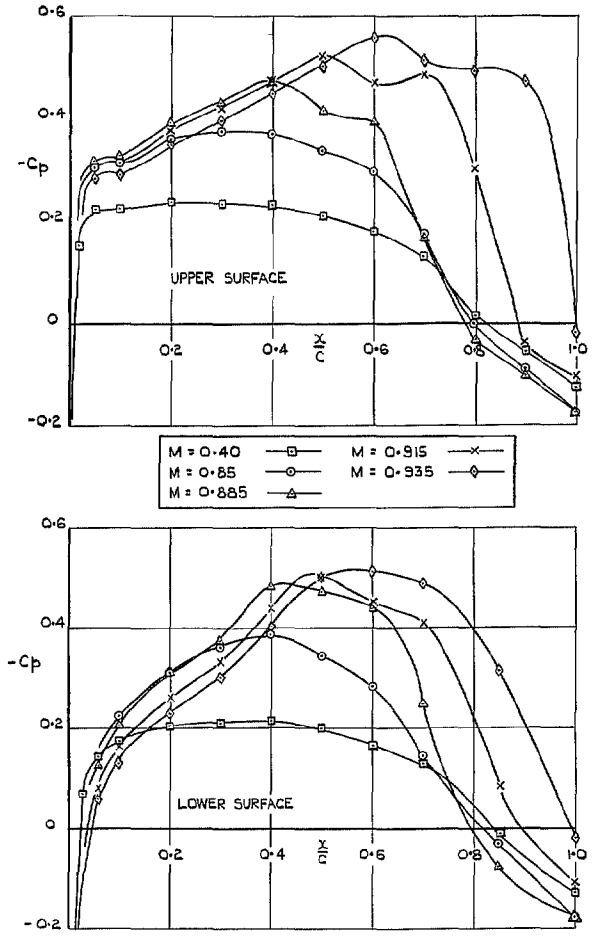

FIG. 12c. Effect of Mach number on the pressure distributions over the wing of the datum model. Section BB ($\eta = 0{\cdot}61$) at $\alpha = 0$ deg.

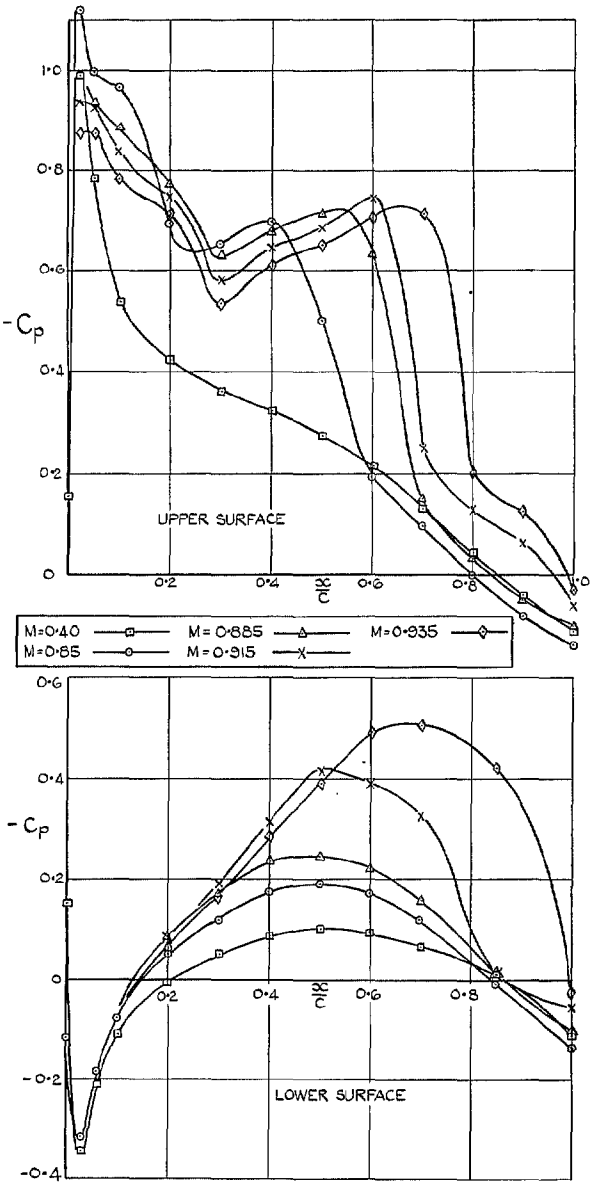

FIG. 12d. Effect of Mach number on the pressure distributions over the wing of the datum model. Section BB ($\eta = 0{\cdot}61$) at $\alpha = 4$ deg.

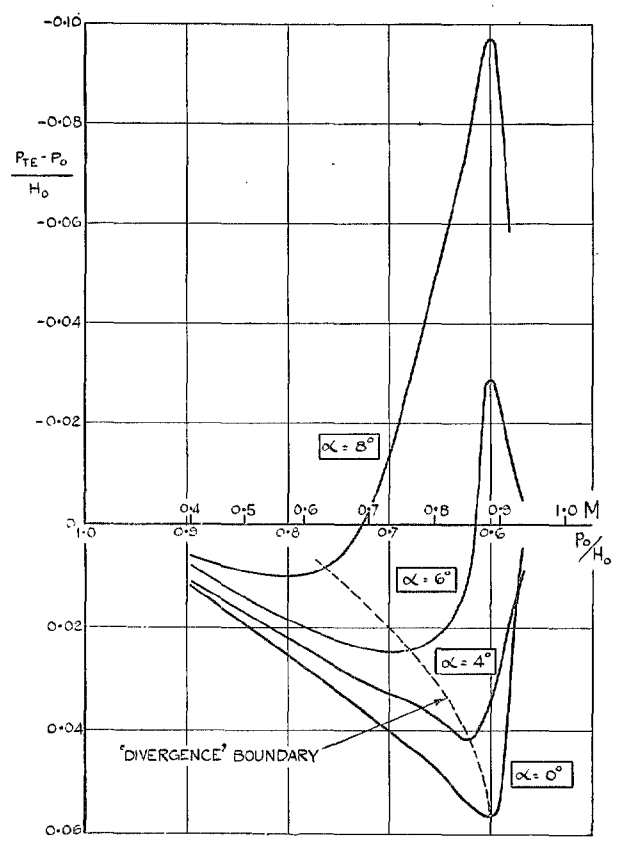

FIG. 13. Variation of trailing-edge pressure with Mach number at constant incidence. Datum-model wing, section BB ($\eta = 0{\cdot}61$).

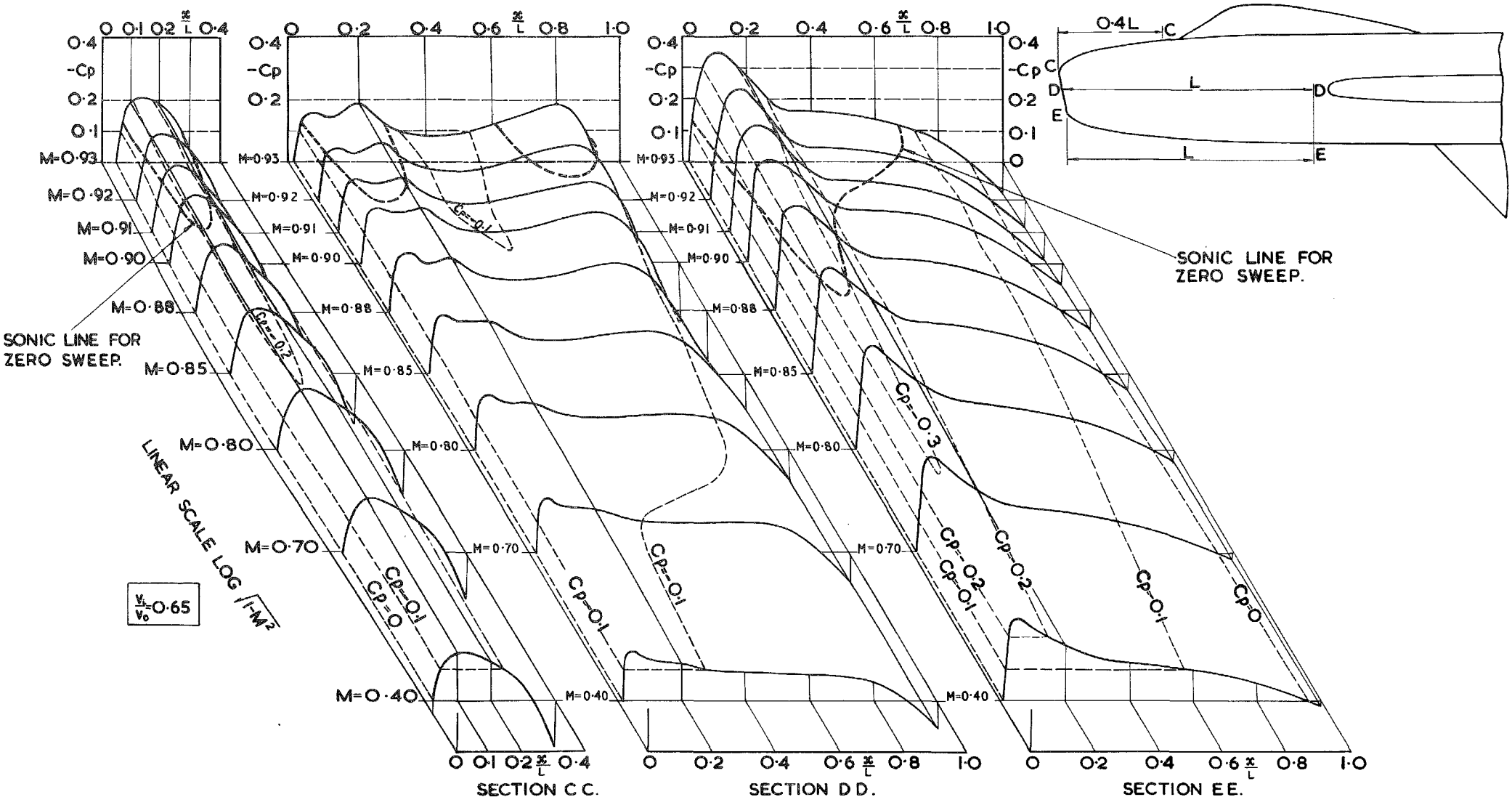
0 0·1 0·2 x/L 0·4
0 0·2 0·4 0·6 x/L 0·8 1·0
-Cp
0·4
0·2
0·1
0
M=0·93
M=0·92
M=0·91
M=0·90
M=0·88
M=0·85
M=0·80
M=0·70
M=0·40
Cp=0·1
Cp=0·2
Cp=0·3
Cp=0
SONIC LINE FOR ZERO SWEEP.
SONIC LINE FOR ZERO SWEEP.
LINEAR SCALE LOG 1/√1-M²
V₁/V₀=0·65
0·4L
C
D
E
L
SECTION C C.
SECTION D D.
SECTION E E.

Fig. 14(a)

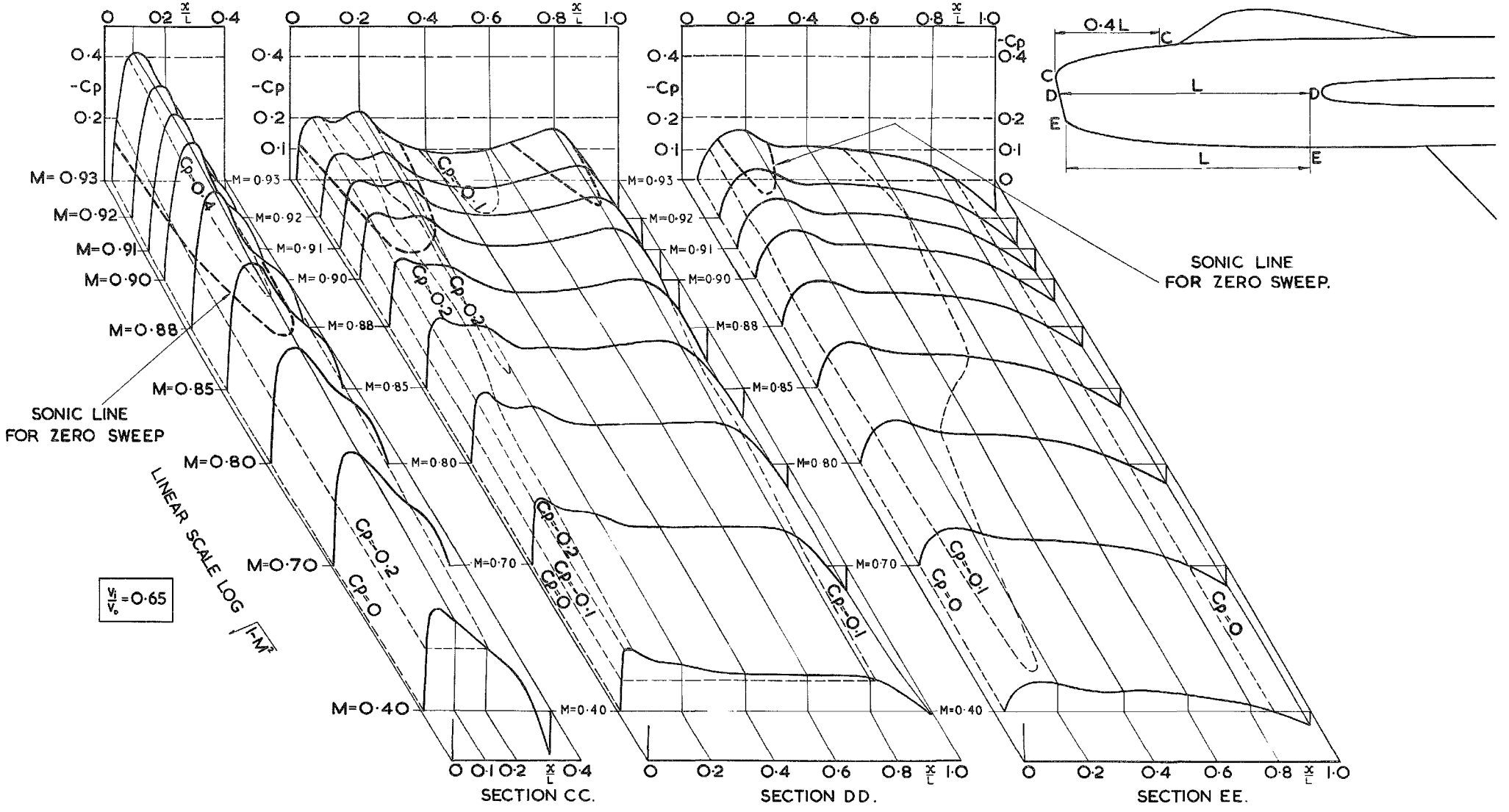
SONIC LINE FOR ZERO SWEEP
SONIC LINE FOR ZERO SWEEP.
LINEAR SCALE LOG √(1-M²)
V₀/V∞ = 0·65
SECTION CC.
SECTION DD.
SECTION EE.
0·4L
C
D
E
L

Fig. 14 (b)

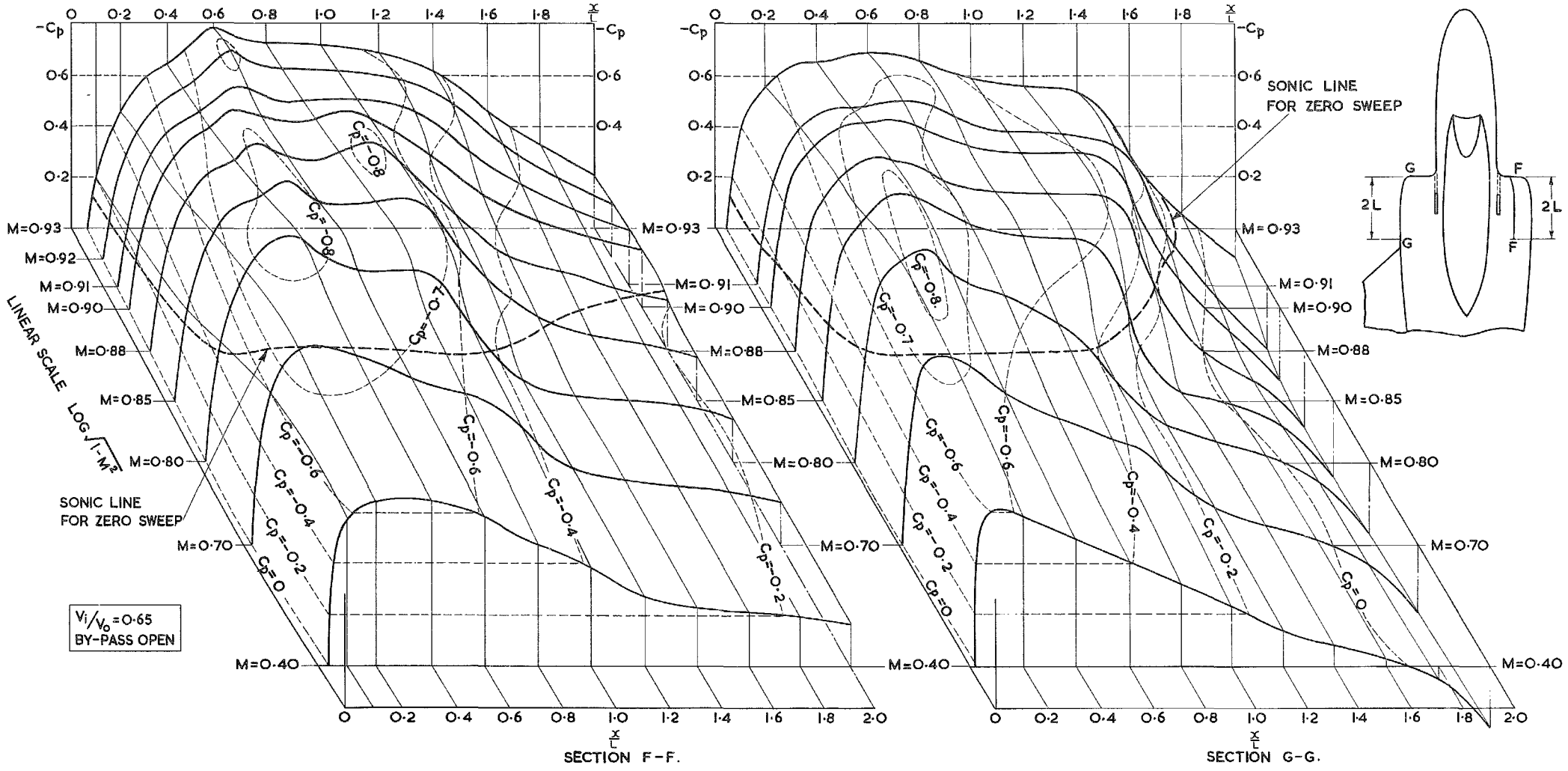
SONIC LINE FOR ZERO SWEEP
LINEAR SCALE LOG $\sqrt{1-M^2}$
$V_i/V_o = 0{\cdot}65$
BY-PASS OPEN
SECTION F-F.
SECTION G-G.
2L
G
F

Fig. 15 (a)

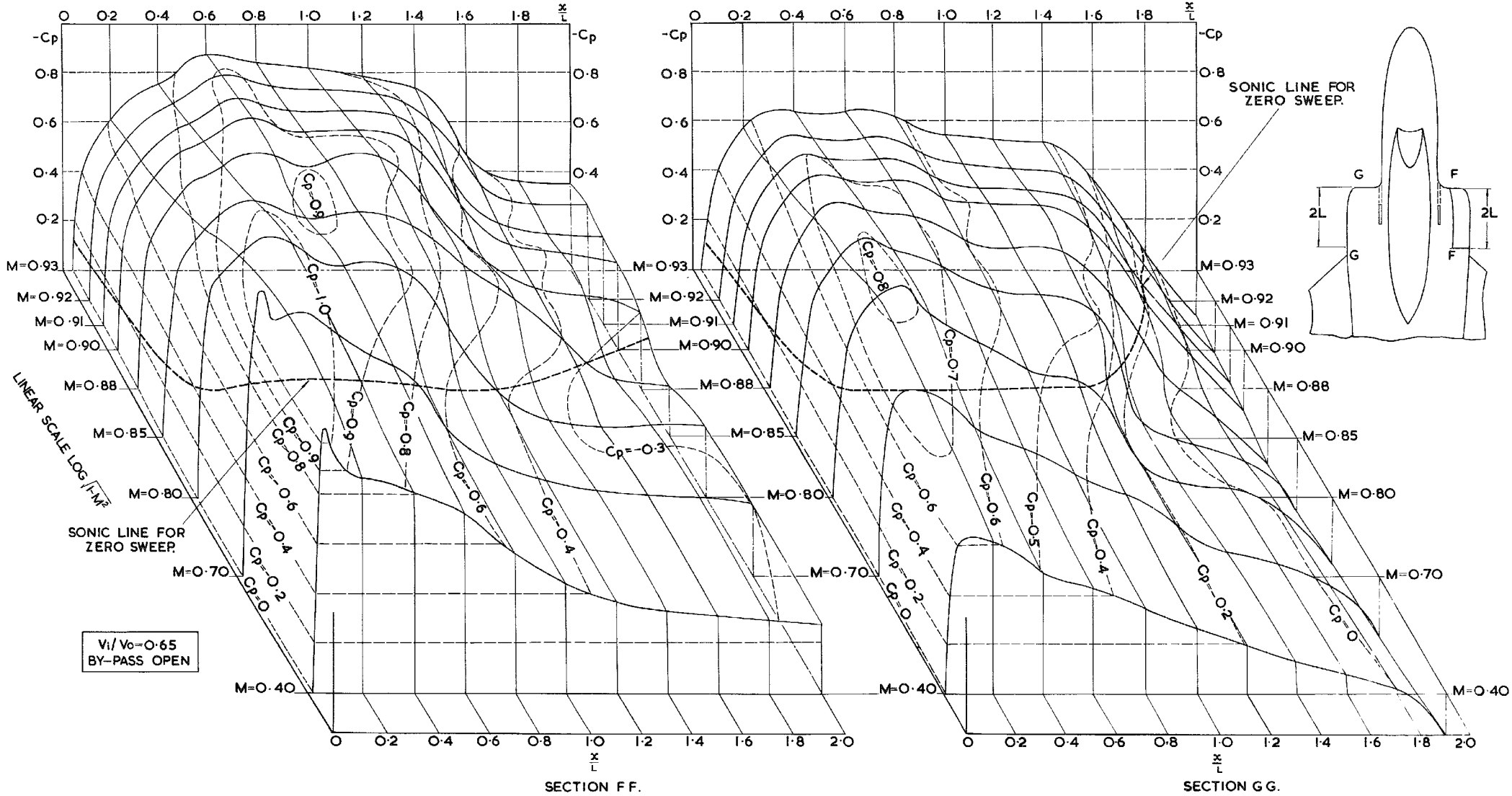
-Cp
x/L
SONIC LINE FOR ZERO SWEEP.
LINEAR SCALE LOG √1-M²
Vi/Vo=0·65
BY-PASS OPEN
SECTION F F.
SECTION G G.
G
F
2L

Fig. 15(b)

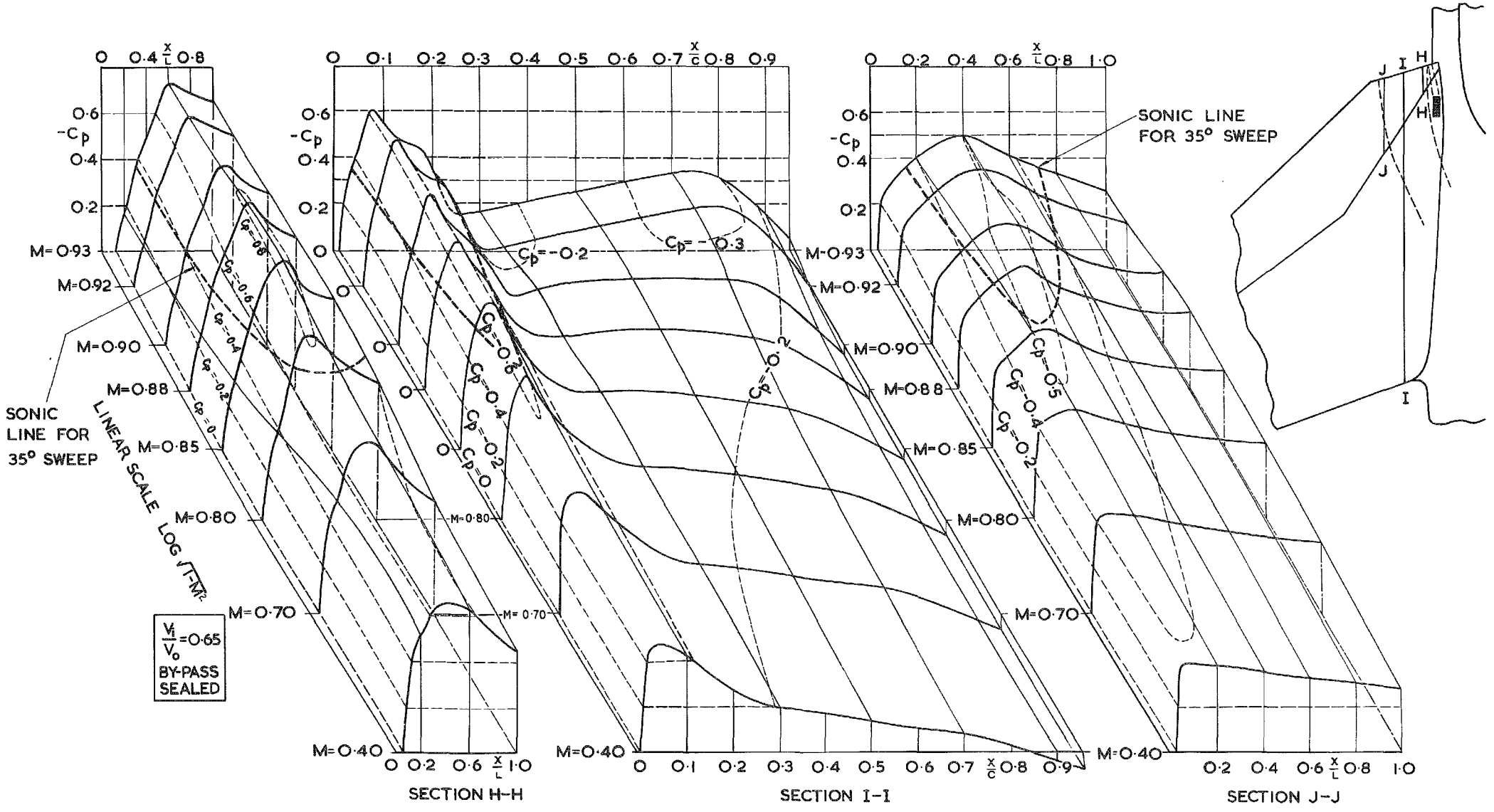
SONIC LINE FOR 35° SWEEP
SONIC LINE FOR 35° SWEEP
LINEAR SCALE LOG $\sqrt{1-M^2}$
$\frac{V_i}{V_o}$=0.65
BY-PASS SEALED
SECTION H-H
SECTION I-I
SECTION J-J
-Cp
M=0·93
M=0·92
M=0·90
M=0·88
M=0·85
M=0·80
M=0·70
M=0·40
Cp=-0·2
Cp=-0·3
Cp=-0·4
Cp=-0·5
Cp=-0·6
Cp=-0·8
Cp=0
H
I
J

Fig. 16(a)

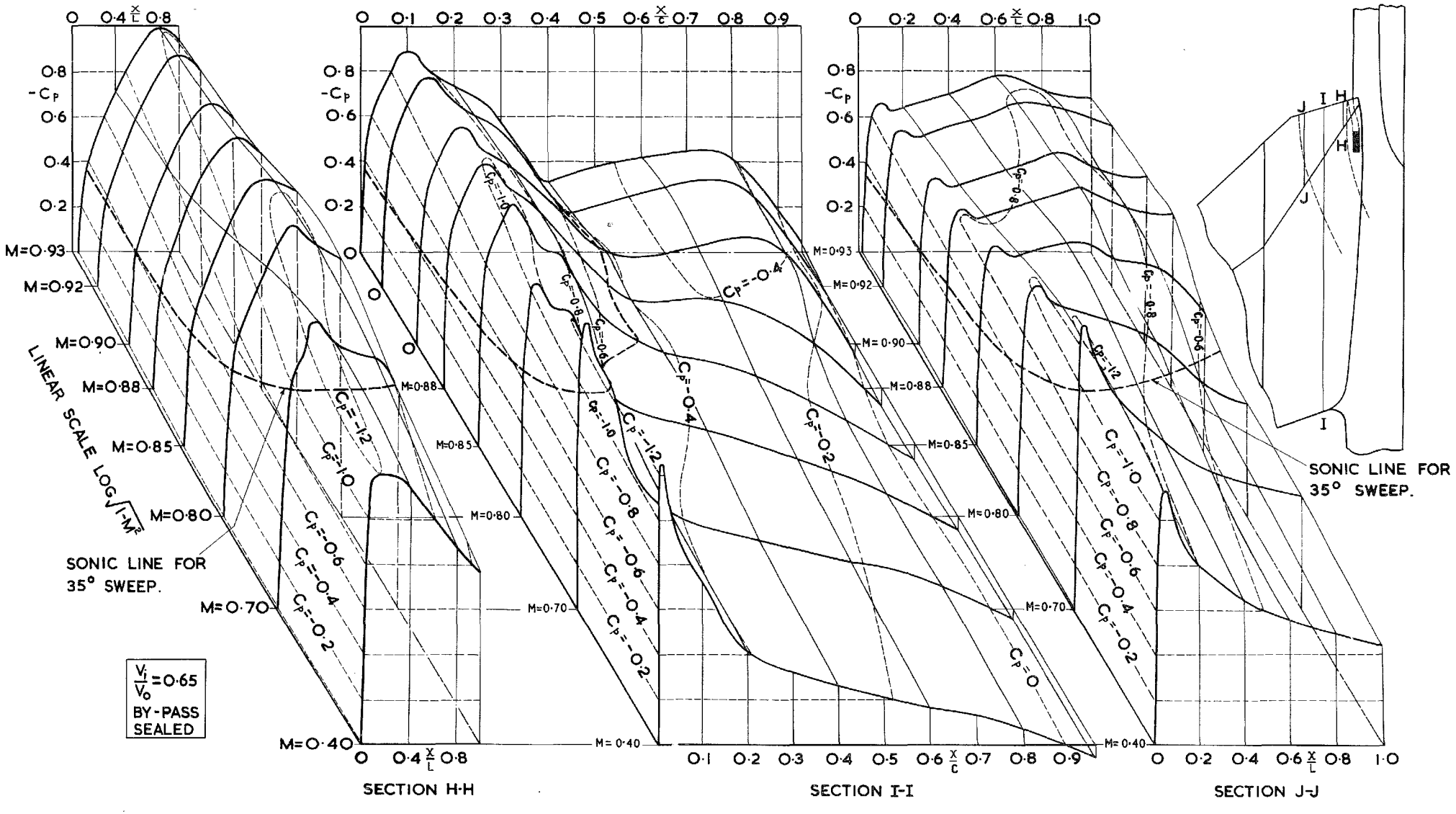

Fig. 16(b)

C.B.H. 32444 · Wt.53-Dd.2293-850-4/59

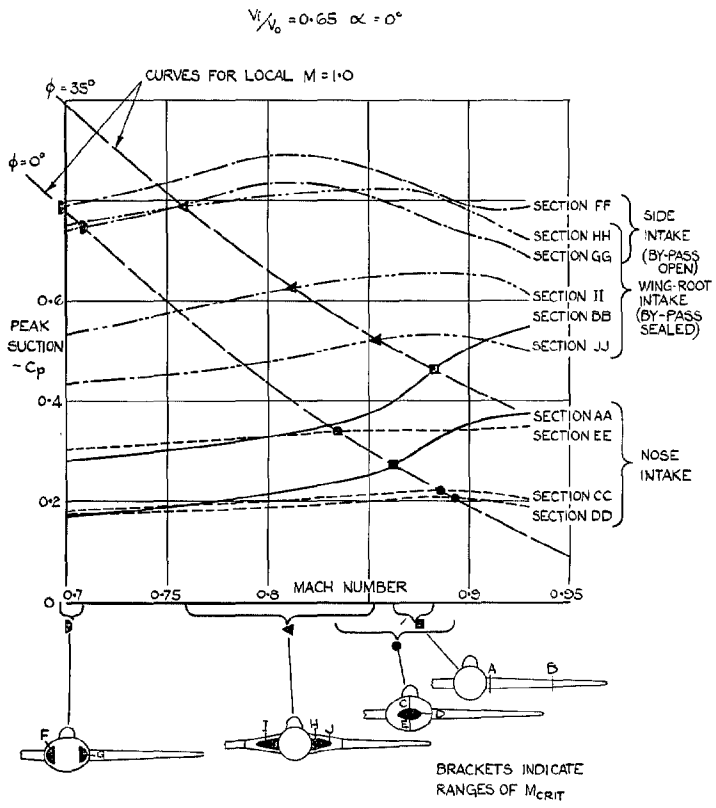

FIG. 17. Variation of measured peak suction with Mach number at $\alpha = 0$ deg, showing critical Mach numbers for the intake fairings. Comparison between the different intake designs.

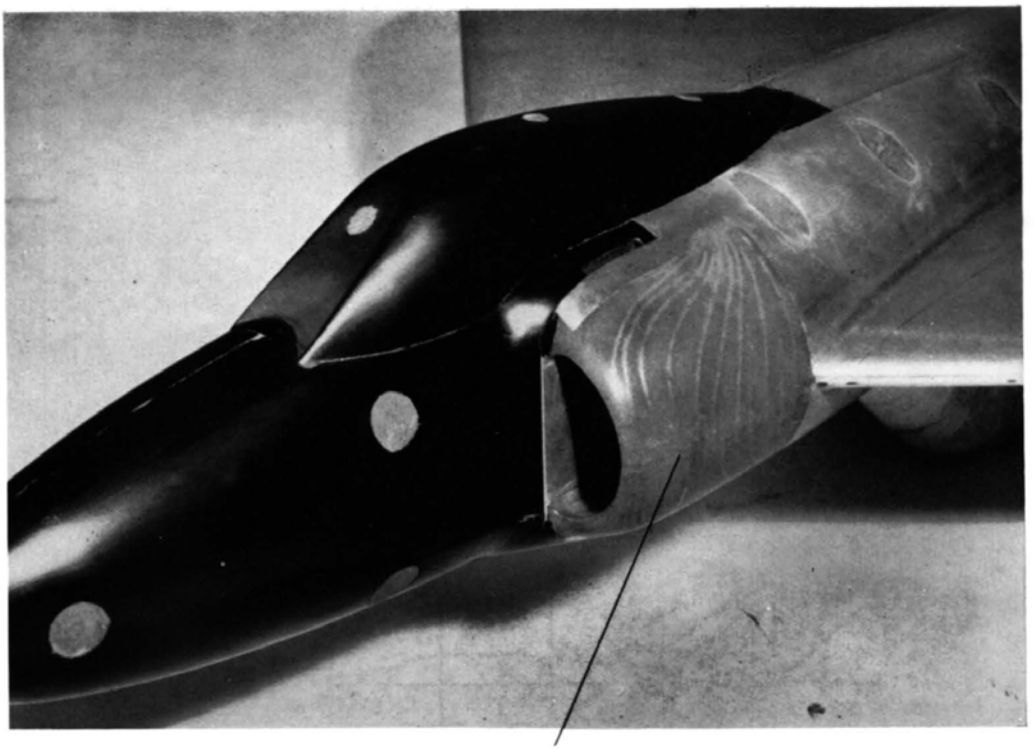

FIG. 18a. Detail of the side-intake boundary-layer by-pass.

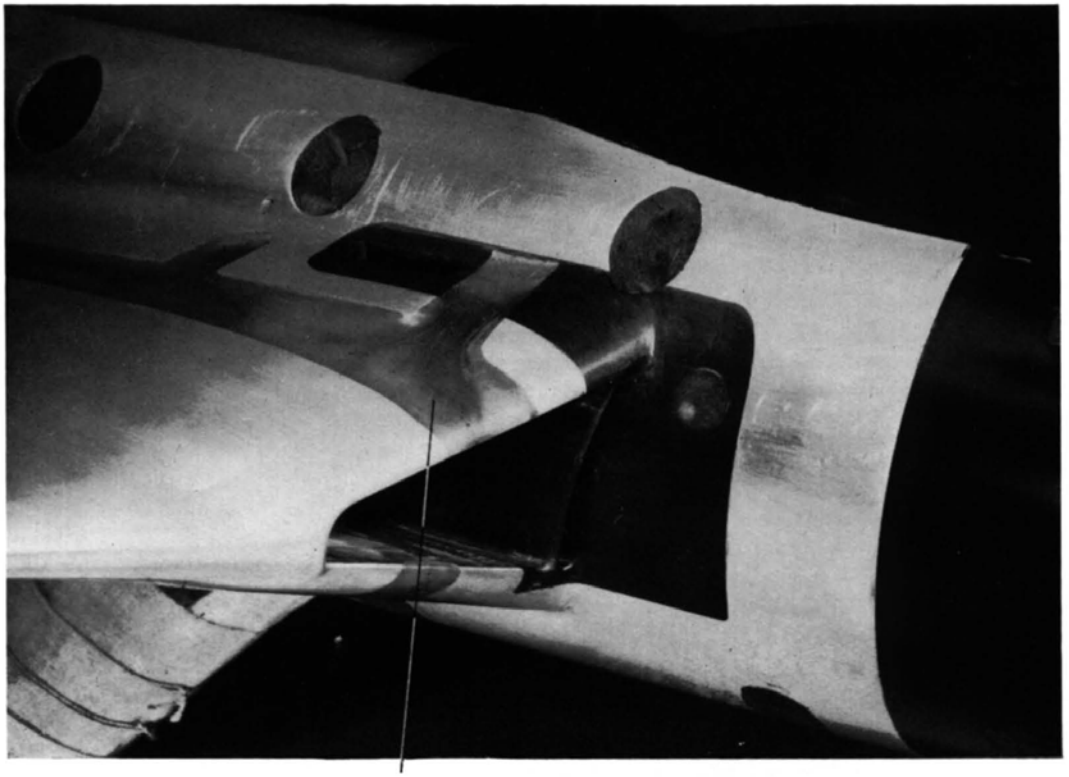

FIG. 18b. Detail of the wing-root intake boundary-layer by-pass.

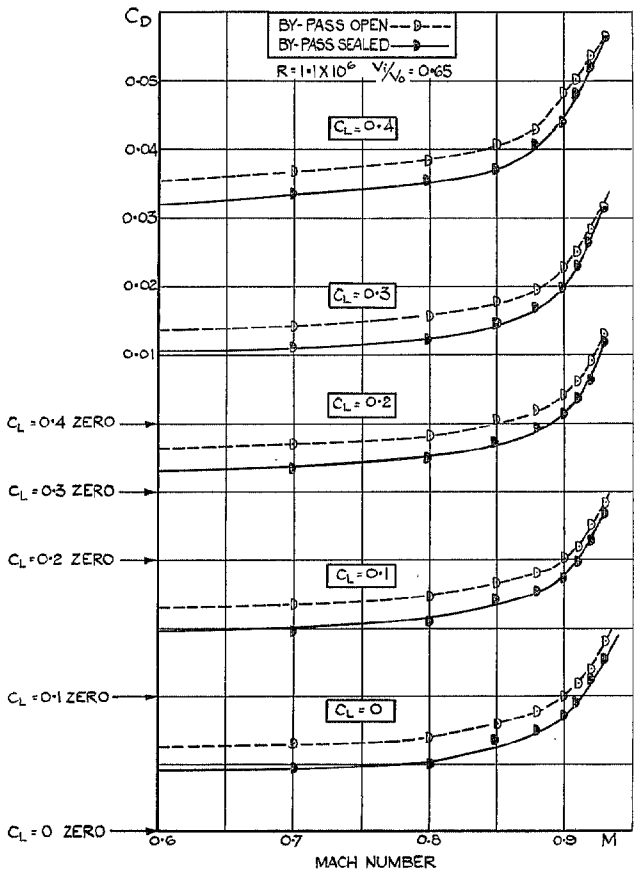

FIG. 19. Effect of sealing boundary-layer by-pass of side intake. Gross C_D *vs.* Mach number at constant C_L.

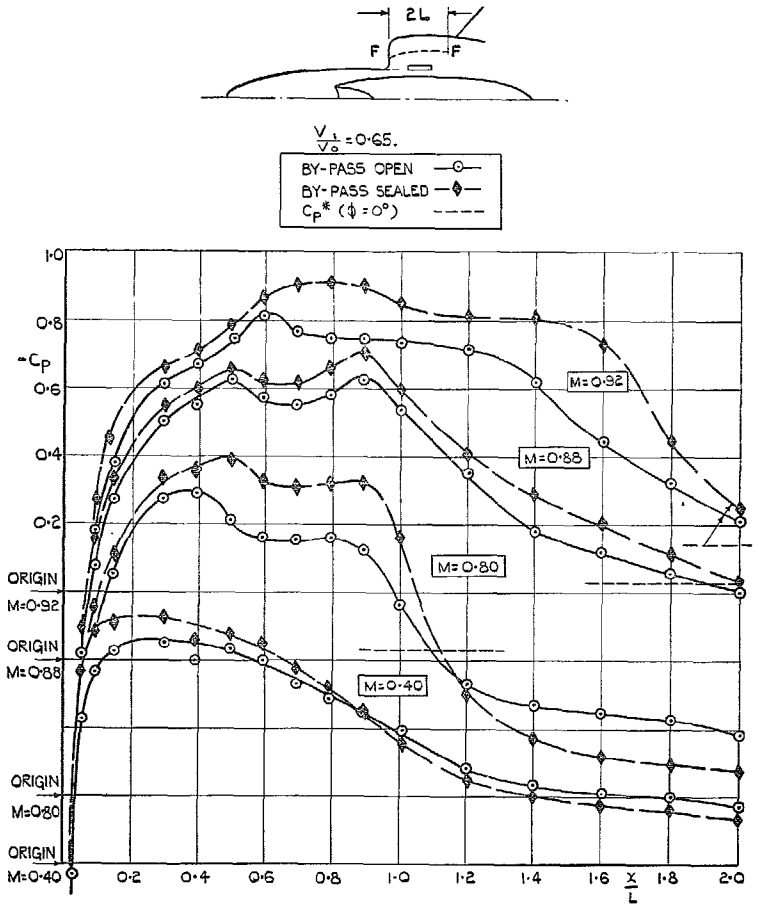

FIG. 20a. Effect of sealing boundary-layer by-pass on pressure distribution over side-intake lip fairing (section FF) $\alpha = 0$ deg.

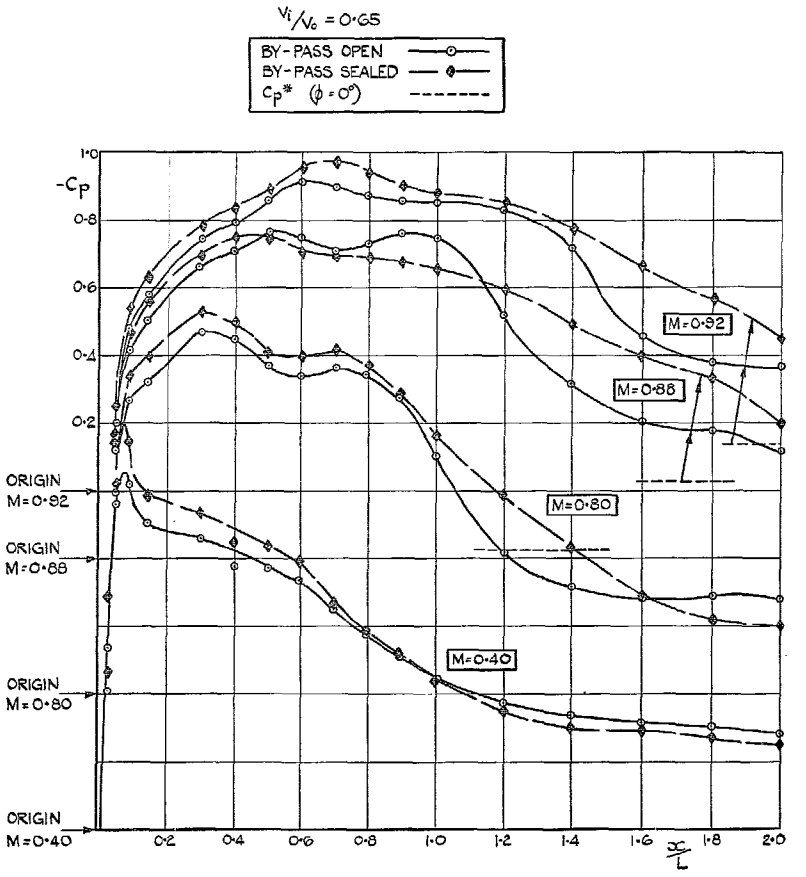

FIG. 20b. Effect of sealing boundary-layer by-pass on pressure distribution over side-intake lip fairing (section FF) $\alpha = 4$ deg.

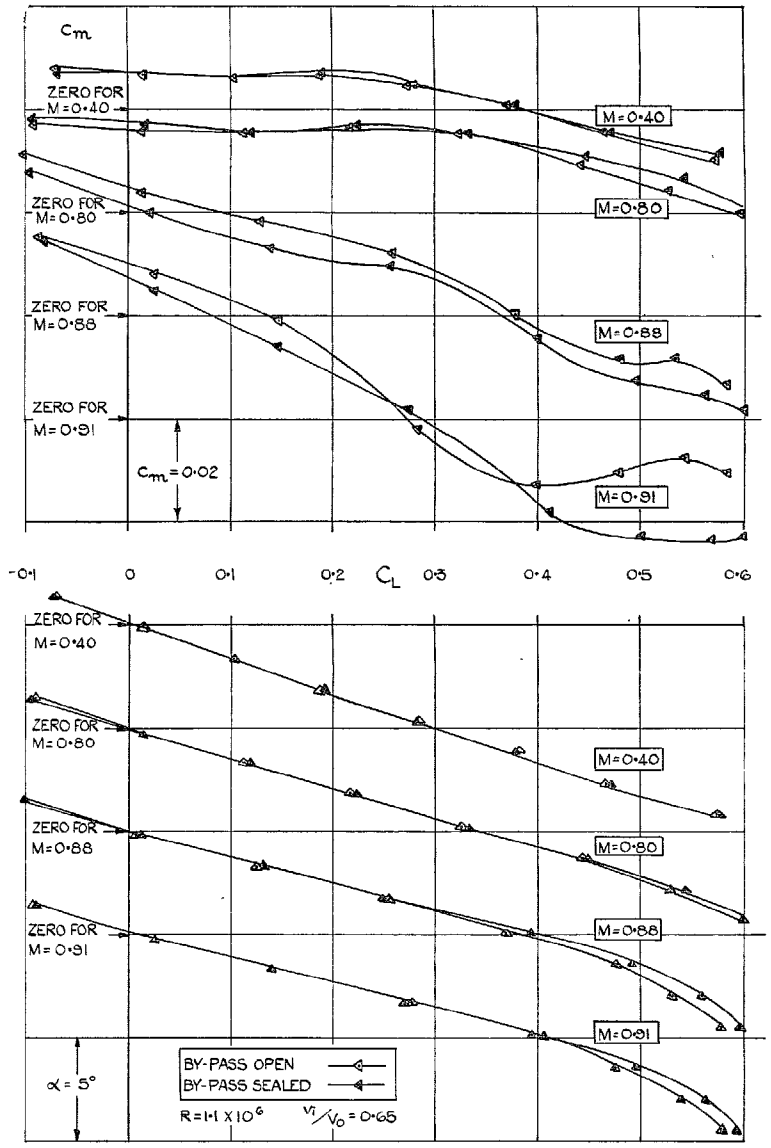

FIG. 21a. Effect of sealing boundary-layer by-pass of wing-root intake. C_m *vs.* C_L, C_L *vs.* α.

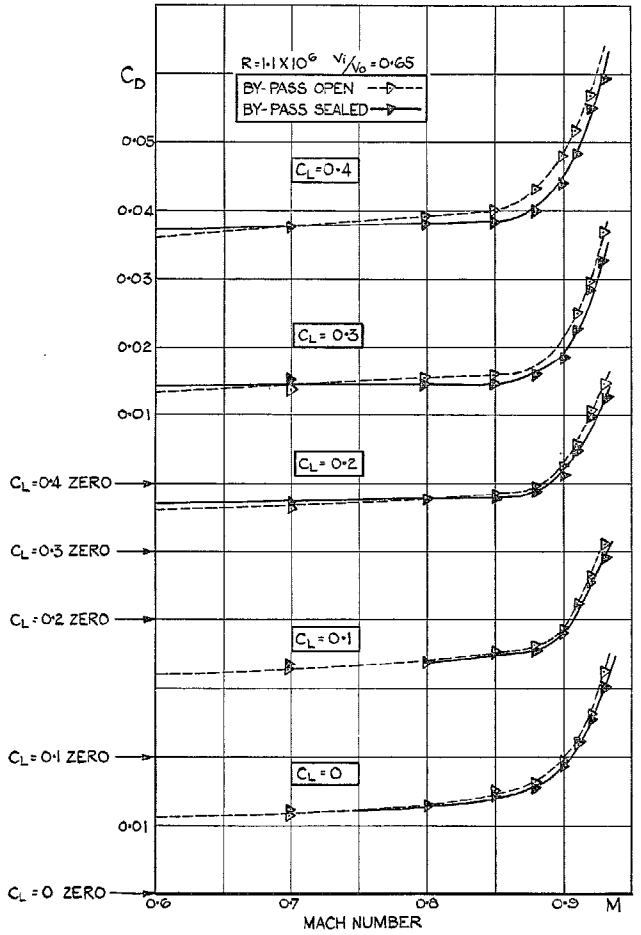

FIG. 21b. Effect of sealing boundary-layer by-pass of wing-root intake. Gross C_D *vs.* Mach number at constant C_L.

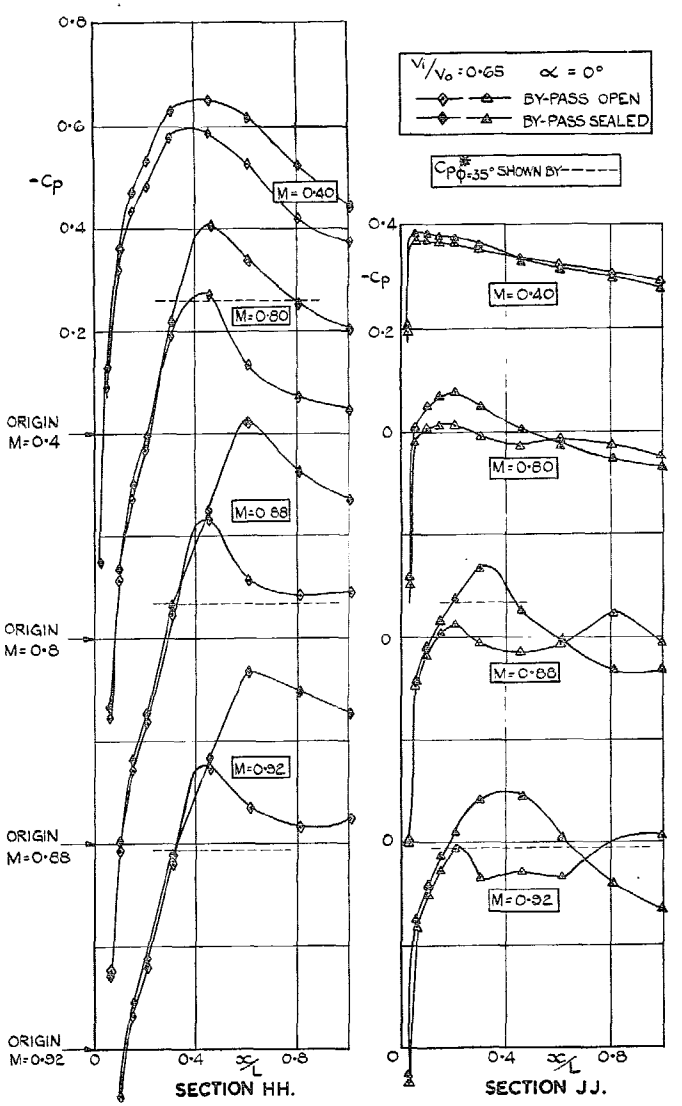

FIG. 22a. Effect of sealing boundary-layer by-pass on pressure distribution over wing-root-intake lip fairings. Sections HH and JJ.

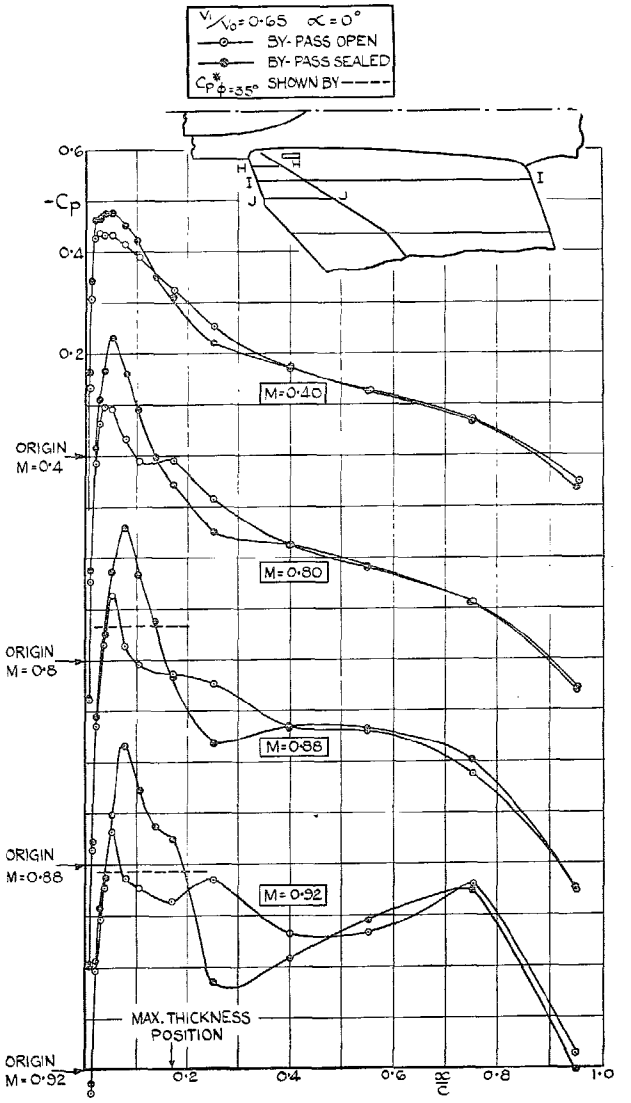

FIG. 22b. Effect of sealing boundary-layer by-pass on pressure distribution over wing-root-intake lip fairings. Section II.

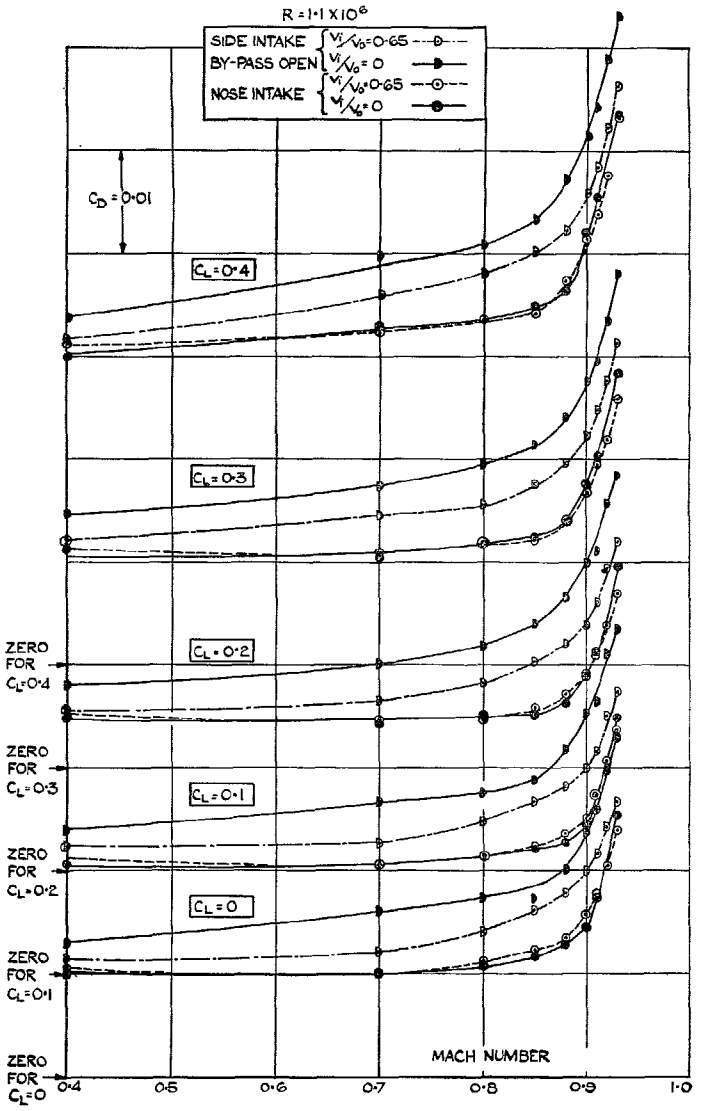

FIG. 23. Effect of velocity ratio on the drag of the nose and side intakes. Gross C_D *vs.* M at constant C_L.

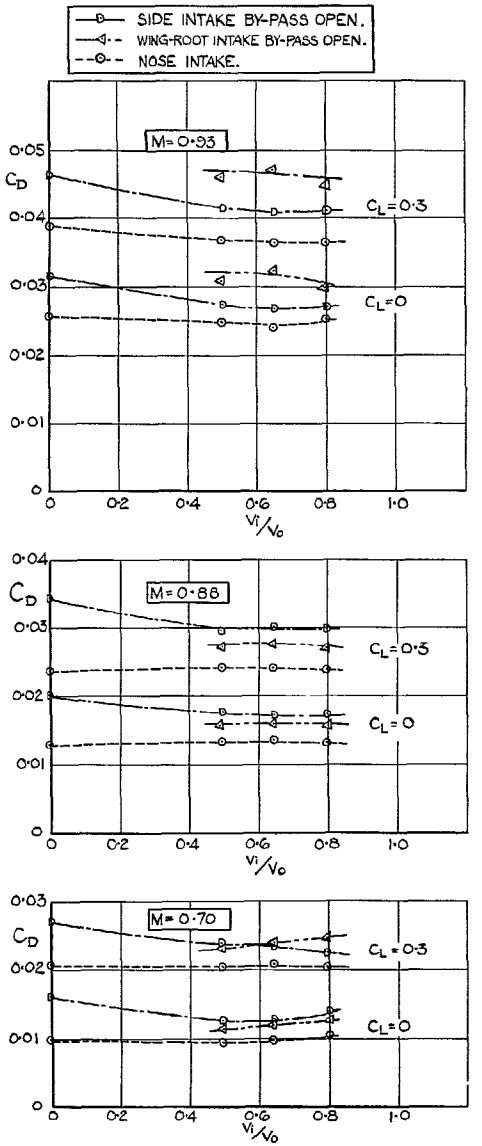

FIG. 24. Effect of velocity ratio on the drag of the three intake designs. Gross C_D *vs.* V_i/V_0.

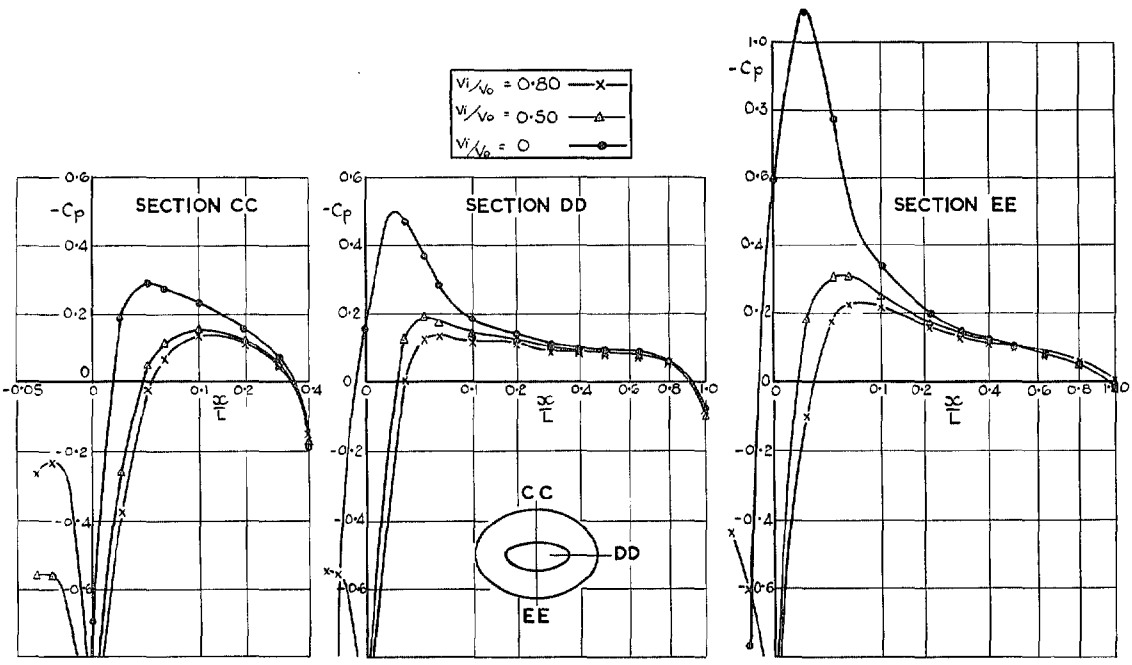

FIG. 25a. Effect of velocity ratio on pressure distribution over the nose intake at $M = 0{\cdot}40$ ($\alpha = 0$ deg).

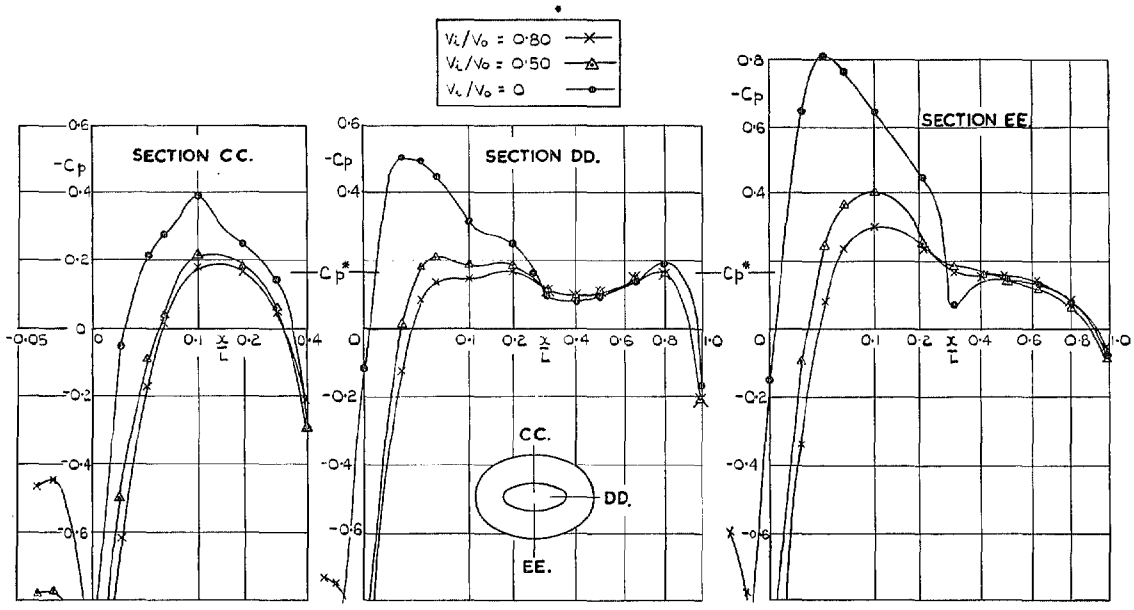

FIG. 25b. Effect of velocity ratio on pressure distribution over the nose intake at $M = 0{\cdot}91$ ($\alpha = 0$ deg).

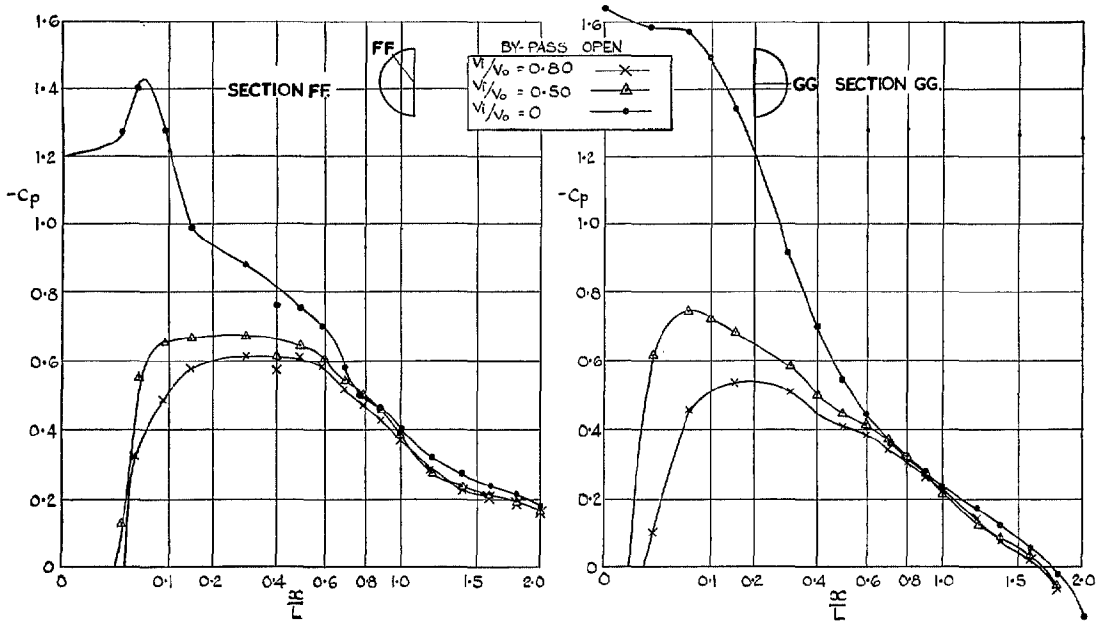

FIG. 26a. Effect of velocity ratio on pressure distribution over the side intake at $M = 0{\cdot}40$ ($\alpha = 0$ deg.)

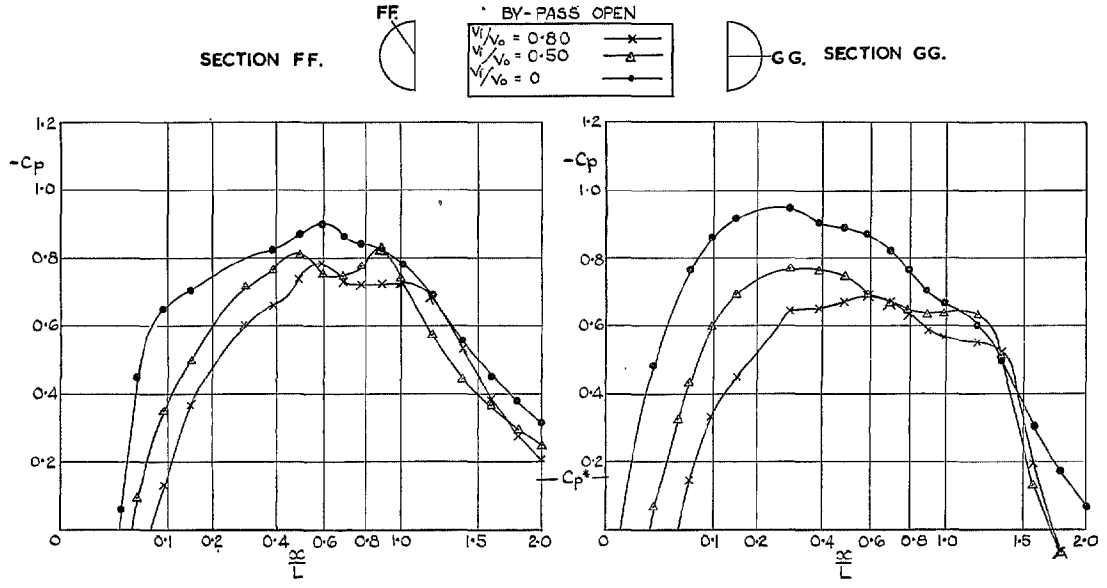

FIG. 26b. Effect of velocity ratio on pressure distribution over the side intake at $M = 0{\cdot}91$ ($\alpha = 0$ deg).

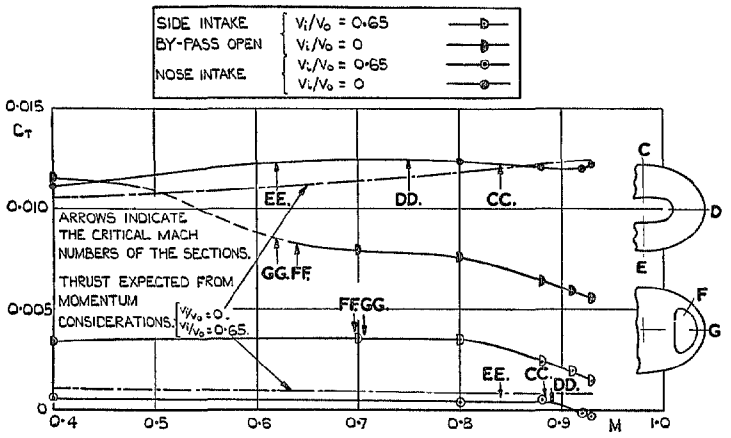

FIG. 27a. Variation with Mach number of thrust from intake fairing of side and nose intakes at two velocity ratios ($\alpha = 0$ deg).

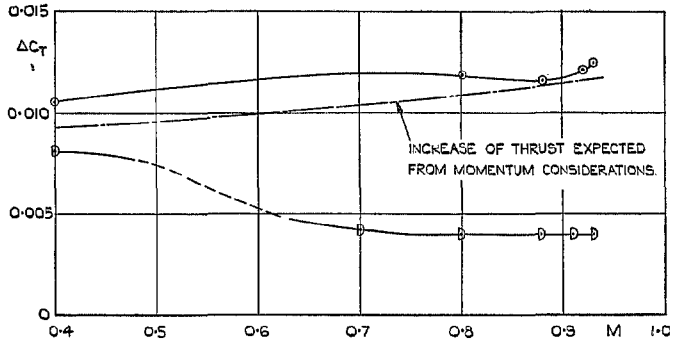

FIG. 27b. Increase in thrust from intake fairing of side and nose intakes due to reduction in velocity ratio from 0·65 to zero ($\alpha = 0$ deg).

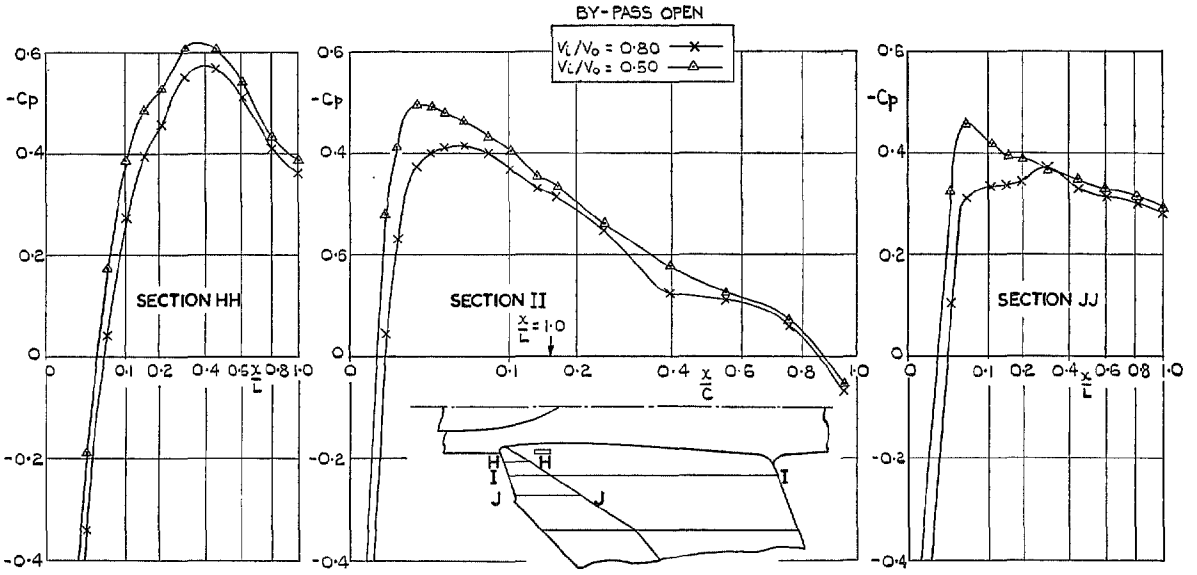

FIG. 28a. Effect of velocity ratio on pressure distribution over the wing-root intake at $M = 0{\cdot}40$ ($\alpha = 0$ deg).

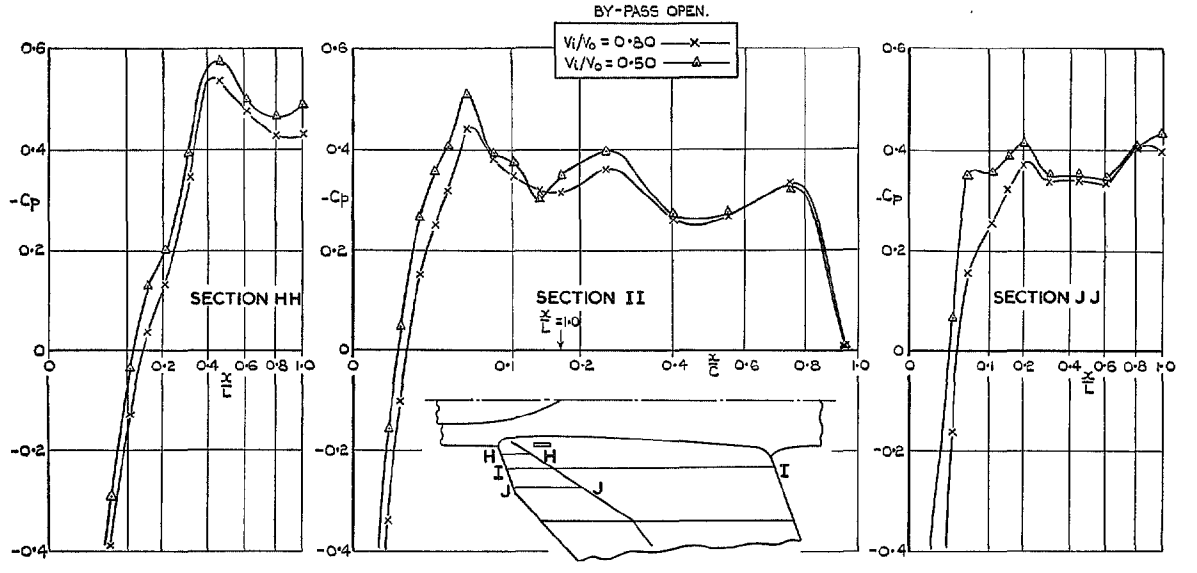

FIG. 28b. Effect of velocity ratio on pressure distribution over the wing-root intake at $M = 0{\cdot}92$ ($\alpha = 0$ deg).

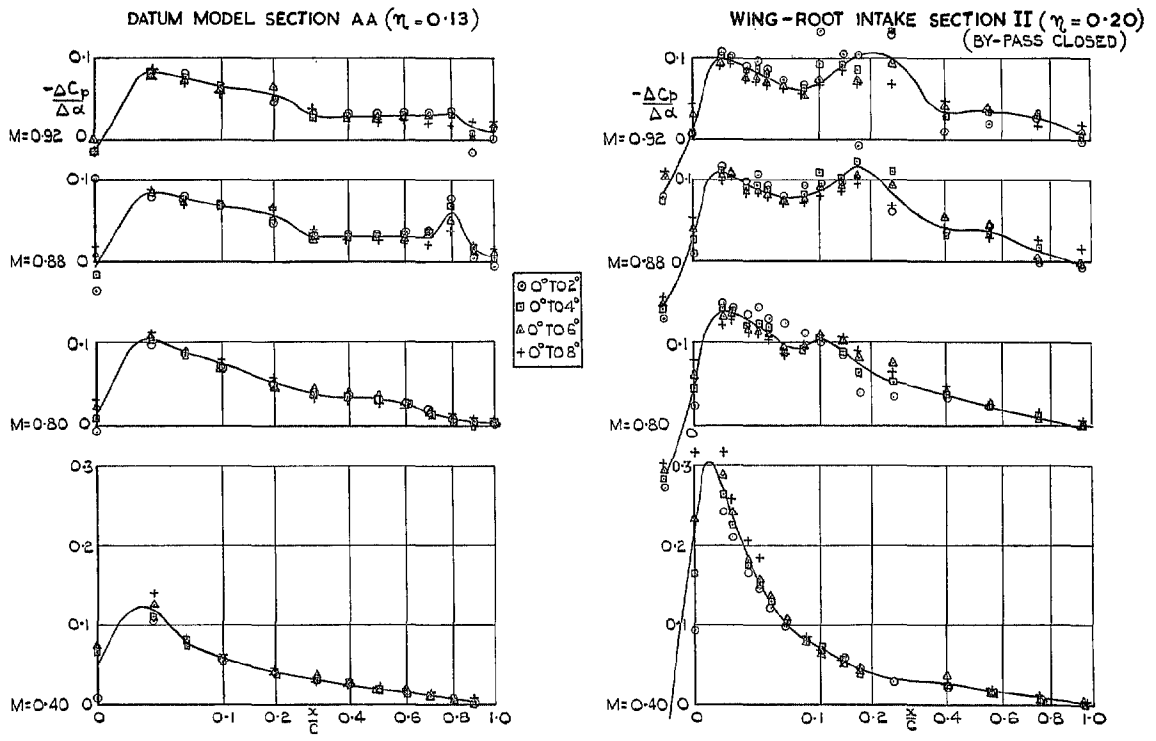

FIG. 29a. Change of upper surface C_p with incidence on datum-model wing and on wing-root intake ($V_i/V_0 = 0{\cdot}65$).

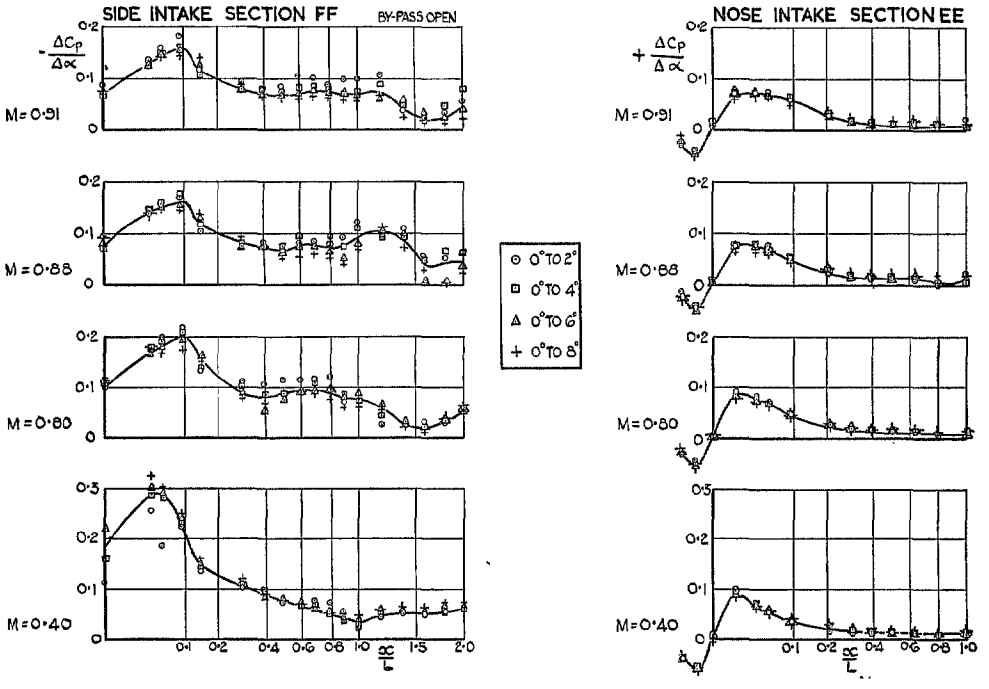

FIG. 29b. Change of C_p with incidence on side and nose-intake lip fairings ($V_i/V_0 = 0{\cdot}65$).

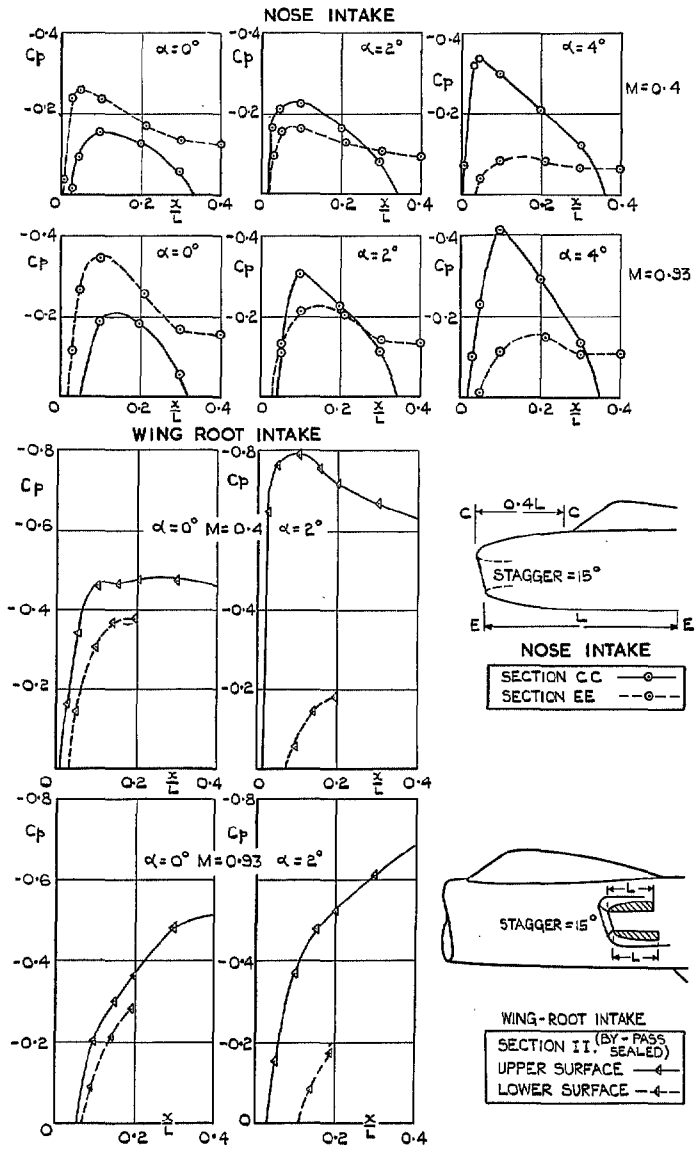

FIG. 30. Effect of stagger on upper and lower surface pressures. Nose and wing-root intakes at $V_i/V_0 = 0{\cdot}65$.

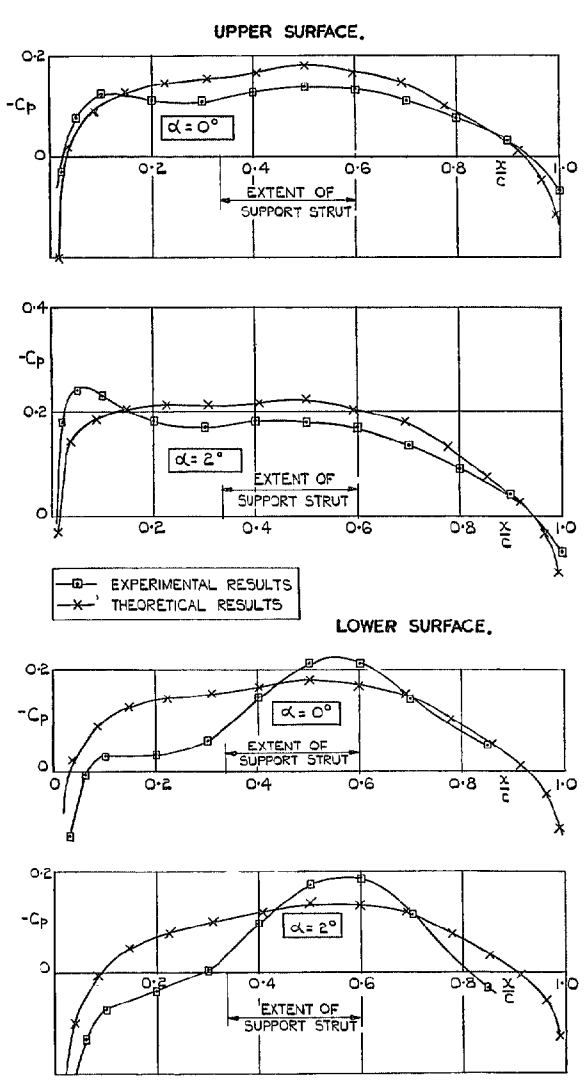

FIG. 31a. Comparison of theoretical ($M = 0$) and experimental ($M = 0{\cdot}4$) pressure distributions on the datum model. Section AA ($\eta = 0{\cdot}13$), $\alpha = 0$ deg and 2 deg.

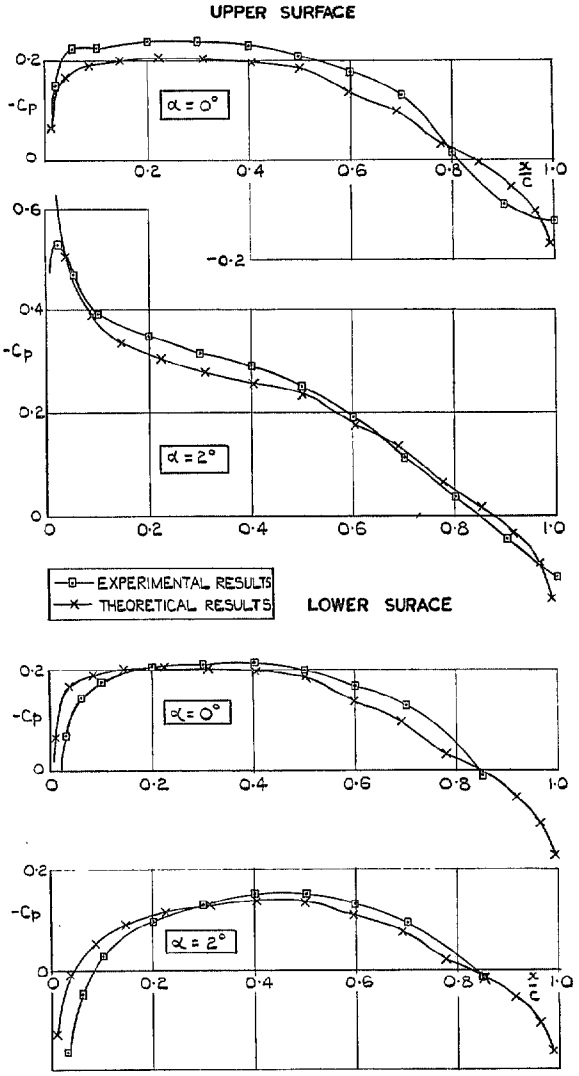

FIG. 31b. Comparison of theoretical ($M = 0$) and experimental ($M = 0{\cdot}4$) pressure distributions on the datum model. Section BB ($\eta = 0{\cdot}61$), $\alpha = 0$ deg and 2 deg.

(76223) Wt. 53/2293 K 7. 6/60 Hw.

PRINTED IN ENGLAND

Publications of the Aeronautical Research Council

ANNUAL TECHNICAL REPORTS OF THE AERONAUTICAL RESEARCH COUNCIL (BOUND VOLUMES)

1939 Vol. I. Aerodynamics General, Performance, Airscrews, Engines. 50*s.* (52*s.*).
Vol. II. Stability and Control, Flutter and Vibration, Instruments, Structures, Seaplanes, etc. 63*s.* (65*s.*)

1940 Aero and Hydrodynamics, Aerofoils, Airscrews, Engines, Flutter, Icing, Stability and Control, Structures, and a miscellaneous section. 50*s.* (52*s.*)

1941 Aero and Hydrodynamics, Aerofoils, Airscrews, Engines, Flutter, Stability and Control, Structures. 63*s.* (65*s.*)

1942 Vol. I. Aero and Hydrodynamics, Aerofoils, Airscrews, Engines. 75*s.* (77*s.*)
Vol. II. Noise, Parachutes, Stability and Control, Structures, Vibration, Wind Tunnels. 47*s.* 6*d.* (49*s.* 6*d.*)

1943 Vol. I. Aerodynamics, Aerofoils, Airscrews. 80*s.* (82*s.*)
Vol. II. Engines, Flutter, Materials, Parachutes, Performance, Stability and Control, Structures. 90*s.* (92*s.* 9*d.*)

1944 Vol. I. Aero and Hydrodynamics, Aerofoils, Aircraft, Airscrews, Controls. 84*s.* (86*s.* 6*d.*)
Vol. II. Flutter and Vibration, Materials, Miscellaneous, Navigation, Parachutes, Performance, Plates and Panels, Stability, Structures, Test Equipment, Wind Tunnels. 84*s.* (86*s.* 6*d.*)

1945 Vol. I. Aero and Hydrodynamics, Aerofoils. 130*s.* (132*s.* 9*d.*)
Vol. II. Aircraft, Airscrews, Controls. 130*s.* (132*s.* 9*d.*)
Vol. III. Flutter and Vibration, Instruments, Miscellaneous, Parachutes, Plates and Panels, Propulsion. 130*s.* (132*s.* 6*d.*)
Vol. IV. Stability, Structures, Wind Tunnels, Wind Tunnel Technique. 130*s.* (132*s.* 6*d.*)

Annual Reports of the Aeronautical Research Council—

1937 2*s.* (2*s.* 2*d.*) 1938 1*s.* 6*d.* (1*s.* 8*d.*) 1939–48 3*s.* (3*s.* 5*d.*)

Index to all Reports and Memoranda published in the Annual Technical Reports, and separately—

April, 1950 - - - - R. & M. 2600 2*s.* 6*d.* (2*s.* 10*d.*)

Author Index to all Reports and Memoranda of the Aeronautical Research Council—

1909—January, 1954 R. & M. No. 2570 15*s.* (15*s.* 8*d.*)

Indexes to the Technical Reports of the Aeronautical Research Council—

December 1, 1936—June 30, 1939	R. & M. No. 1850	1*s.* 3*d.* (1*s.* 5*d.*)
July 1, 1939—June 30, 1945	R. & M. No. 1950	1*s.* (1*s.* 2*d.*)
July 1, 1945—June 30, 1946	R. & M. No. 2050	1*s.* (1*s.* 2*d.*)
July 1, 1946—December 31, 1946	R. & M. No. 2150	1*s.* 3*d.* (1*s.* 5*d.*)
January 1, 1947—June 30, 1947	R. & M. No. 2250	1*s.* 3*d.* (1*s.* 5*d.*)

Published Reports and Memoranda of the Aeronautical Research Council—

Between Nos. 2251–2349	R. & M. No. 2350	1*s.* 9*d.* (1*s.* 11*d.*)
Between Nos. 2351–2449	R. & M. No. 2450	2*s.* (2*s.* 2*d.*)
Between Nos. 2451–2549	R. & M. No. 2550	2*s.* 6*d.* (2*s.* 10*d.*)
Between Nos. 2551–2649	R. & M. No. 2650	2*s.* 6*d.* (2*s.* 10*d.*)
Between Nos. 2651–2749	R. & M. No. 2750	2*s.* 6*d.* (2*s.* 10*d.*)

Prices in brackets include postage

HER MAJESTY'S STATIONERY OFFICE

York House, Kingsway, London W.C.2; 423 Oxford Street, London W.1; 13a Castle Street, Edinburgh 2; 39 King Street, Manchester 2; 2 Edmund Street, Birmingham 3; 109 St. Mary Street, Cardiff; Tower Lane, Bristol 1; 80 Chichester Street, Belfast, *or through any bookseller.*

S.O. Code No. 23-3134